This is a preprint, the final version is subject to change, of the American Mineralogist (MSA)
Cite as Authors (Year) Title. American Mineralogist, in press.
(DOI will not work until issue is live.) DOI: http://dx.doi.org/10.2138/am-2017-6003

Revision 1

Study on structure variations of incommensurately modulated labradorite feldspars with different cooling histories

Shiyun Jin and Huifang Xu

NASA Astrobiology Institute, Department of Geoscience, University of Wisconsin–Madison, Madison, Wisconsin 53706, United States

* Corresponding author:
Dr. Huifang Xu, Professor
Department of Geoscience,
University of Wisconsin-Madison
608-265-5887 (O)
hfxu@geology.wisc.edu

This is a preprint, the final version is subject to change, of the American Mineralogist (MSA)
Cite as Authors (Year) Title. American Mineralogist, in press.
(DOI will not work until issue is live.) DOI: http://dx.doi.org/10.2138/am-2017-6003

Abstract

The incommensurately modulated structures of three intermediate plagioclase feldspars with compositions of ~An_{51} are determined by single crystal X-ray diffraction analyses. The samples selected cover a range of different cooling rate, from relatively fast to extremely slow. The structures show various ordering states that are directly correlated with the cooling histories of the samples. The slowest cooled sample shows an *e*1 structure with strong density modulation, along with nanoscale exsolution lamellae. The fastest cooled sample displays an *e*2 structure, without second-order satellite reflections (*f*-reflections) and density modulation. The sample with intermediate cooling rate shows a less ordered *e*1 structure with weak density modulation, but the modulation period and orientation are the same as in *e*2 structure. The comparison of the structures with the same composition reveals the ordering process and phase transitions during the cooling of plagioclase within the compositional range of Bøggild intergrowth. New parameters from modulation waves can be used for quantifying the ordering state of plagioclase feldspars. Proposed phase relationship and T-T-T diagram for ~An_{51} plagioclase feldspars are illustrated for explaining the relationship among $C\bar{1}$, *e1* and *e2* structures and relative cooling rates of their host rocks.

Keywords: labradorite, incommensurate, modulated structure, density modulation, gabbro, *e*-plagioclase, cooling rate, ordering state, exsolution lamellae, intermediate plagioclase

Introduction

Plagioclase feldspar ($Ca_xNa_{1-x}Si_{3-x}Al_{1+x}O_8$), a coupled solid solution between albite ($NaAlSi_3O_8$) and anorthite ($CaAl_2Si_2O_8$), is the most abundant group of minerals in the Earth's crust. The intermediate labradorite feldspars (An_{50}~An_{70}) are common in mafic rocks. Plagioclase with composition between ~An_{25} to ~An_{75} often show satellite diffractions (*e*-reflections) surrounding the absent *b*-reflections, indicating an incommensurately modulated structure (Bown and Gay 1959; Ribbe 1983a; Smith and Brown 1988). The aperiodic structure of intermediate plagioclase at low temperature and its complicated subsolidus phase relations have puzzled mineralogists and petrologists for more than 70 years. Many structure models of the aperiodic structure have been proposed and refuted since the discovery of aperiodic plagioclase (Chao and Taylor, 1940). Recent Z-contrast imaging study indicates polarity of the structure in a bytownite sample by Xu (2015), and is confirmed by a high quality structure refinement of a metamorphic labradorite sample by Jin and Xu (2017). The structure of *e*-plagioclase is composed of periodic $I1$ like domains connected by inversion twin boundaries, instead of $I\bar{1}$ domains related by antiphase boundaries.

Incommensurately modulated structures are quite common in nature, and have been an important subject of crystallography for a long time. The modulated structure consists of a lattice periodic basic structure and a periodic modulation (Janssen et al. 2007). The structure of each unit cell of the basic lattice structure is modified by the modulation function from one to the next. The structure is incommensurate when the ratio between the modulation period and the basic unit cell length is an irrational number. As the modulation function would never meet the basic lattice structure at the same point, the whole structure become aperiodic. The aperiodicity would be reflected in reciprocal space by satellite reflections that cannot be indexed with three integer numbers. An extra dimension has to be introduced for describing incommensurately modulated structure, where each parameter of the structure (occupancies, coordinates) is described by a periodic function. Characterization of incommensurately modulated structure in (3+1)D space is a fully developed theory (van Smaalen 2007; Wagner and Schoenleber 2009), and powerful and user-friendly software is available (Petříček et al. 2014).

Despite recent studies, many questions about the phase relations remain unsolved. The incommensurately modulated plagioclase, or *e*-plagioclase, has been categorized into two types,

77 *e*1 and *e*2, based on the existence of second order satellite reflections, or *f*-reflections (Ribbe,
78 1983b; Smith, 1984; Carpenter, 1994; McConnell, 2008). In the diffraction pattern of an *e*1
79 structure, not only can the *e*-reflections surrounding the absent *b*-positions be observed, but also
80 second order satellite reflections, *f*-reflections appear around the main *a*-reflections; whereas in
81 *e*2 structure, only the first order satellites, *e*-reflections are present. Almost all previous samples
82 studied by single crystal X-ray diffraction were *e*1 with observable *f*-reflections. Little is known
83 about the other category, the *e*2 structure, since only one structure refinement was done on this
84 structure (Steurer and Jagodzinski 1988). The *e*1 structure is normally believed to only exist in
85 the Ca-rich plagioclase (Ribbe, 1983b; Smith, 1984; Smith and Brown, 1988), but Xu *et al.*
86 (2016) discovered a plagioclase sample with a composition of ~An_{45} that displays *e*1 structure,
87 which makes the case more complicated. It was proposed that the $C\bar{1}\rightleftharpoons e2$ transition might be
88 thermodynamically continuous, even though the transition temperature is too low to make it
89 reversible in the lab (Carpenter, 1986). This makes the relationship between *e*1 and *e*2 structure
90 more problematic: is the difference between these two structures large enough to create a
91 miscibility gap between them, or are they essentially the same phase, with only gradually
92 decreasing intensities of satellite reflections?

93 The structure refinement of the labradorite from a metamorphic rock (Jin and Xu, 2017) reveals
94 the ordering pattern of *e*-plagioclase in another dimension, which opens the door to a whole new
95 level of understanding the ordering states of plagioclase. Instead of using only average Al
96 occupancy of T_1o site, the modulation of T-O bond distances, Ca-Na occupancies and density
97 modulation could all be used for quantifying the ordering state of the structure with much higher
98 sensitivity and accuracy. However, an individual structure of this composition can only provide
99 us the stability state of *e*-plagioclase, but nothing about the phase transition and ordering
100 mechanism. As the diffusion between Al and Si within the crystal lattices is extremely difficult
101 (Grove *et al.*, 1984; Liu and Yund, 1992), which makes experiments for these phase transitions
102 impractical in the laboratory, such information can only be preserved in plagioclase of igneous
103 origin with a composition within the range of Bøggild intergrowth. In this paper, three carefully
104 chosen igneous plagioclase samples with modulated structure are analyzed with single crystal X-
105 ray diffraction. The comparison between the samples with similar composition but different
106 cooling histories would provide important information about the phase transitions as well as

ordering mechanism of intermediate plagioclase, which are critical for mapping out the phase relations around the composition range of Bøggild intergrowth.

Samples and Experiments

Three plagioclase samples of igneous origin with similar composition (~ An_{51}) but different cooling histories were analyzed in this study. All samples were carefully characterized using selected-area electron diffraction (SAED), dark-field TEM imaging, and electron microprobe analysis (EMPA) before they were used for single crystal X-ray diffraction analyses. Details about the compositions of the samples are listed in Supplementary Table. K-feldspar component in the samples are low (~2 mole% of Or).

Sample Dul-15-8B is a melanogranophyre intrusion in the anorthositic layer of the Duluth Igneous Complex. The sample was collected from a roadcut on Skyline Parkway on the south side of Twin Ponds swimming area (Stop 1-8 in Miller's (2009) field guide). The intrusion is considered to have formed from late-stage melts fluxing through the intercumulus pore spaces of the partially molten anorthositic series of the Duluth Layered Complex (Miller, 2009). The intrusion is very small, with a diameter of only about 1 km at the current level of exposure, indicating a relatively fast cooling rate with respect to the main body of the Layered Complex (Miller, 2009). The TEM image of the sample shows a homogeneous crystal with no exsolution lamellae. The electron diffraction pattern shows definite yet weak *e*-reflections, but no *f*-reflections are observed (Fig. 1). The plagioclase in the sample shows a relatively large variation in composition from crystal to crystal, from ~An_{50} to ~An_{57}.

Sample SK90-12 is from Lower Zone C (top of lower zone) of the Skaergaard layered intrusion, which is similar to the Duluth igneous complex in many respects (Taylor, 1964). The size of the intrusion is about 10 km across (Nielsen, 2004; Winter, 2010). Plagioclase crystals in this layer are quite homogeneous from core to rim with a composition of ~An_{50} (Toplis *et al.*, 2008). No exsolution lamellae are observed by TEM (Fig. 2). First-order satellite reflections (*e*-reflections) are sharp. Second-order satellite reflections (*f*-reflections) are weak in SAED patterns (Fig. 2). Plagioclase from the Skaergaard intrusion are classic samples and have been subjected to extensive analyses for their incommensurate structures (Gay, 1956; Carpenter, 1986, 1994). No sign of exsolution was reported in any previous work.

Sample R2923 is an iridescent labradorite crystal from the collection of Smithsonian National Museum of Natural History, Washington, DC. The sample shows red to dark orange iridescent

color, indicating nanoscale exsolution lamellae resulted from extremely slow cooling. TEM images (Fig. 3) show almost periodic exsolution lamellae with alternating thickness. Based on EDS results, the wide lamellae are more Ca-rich than the thin lamellae. The compositions are about An_{54} and An_{48} respectively. The minor change of modulation direction across adjacent lamellae indicates the difference in structure should be relatively small. The electron diffraction pattern (Fig. 3**B**) also shows only sharp round satellites instead of splitting peaks. Iridescent labradorite feldspars are only found in slowly cooled gabbroic or anorthositic massifs (Smith and Brown, 1988). As the diffusion between Al and Si is extremely sluggish at low temperature (Grove *et al.*, 1984; Liu and Yund, 1992), the rather coarse exsolution lamellae in sample R2923 prove extremely slow cooling of the host rock.

The composition of the samples was analyzed by electron microprobe around the areas on the thin section with thick albite twin lamellae for selecting crystals for X-ray diffraction. Sample Dul-15-8B and SK90-12 were analyzed with a CAMECA SXFive-FE at 15kV and 10nA beam current with a 10-micron beam size. Sample R2923 were analyzed with a CAMECA SX51 microprobe at 15 kV and 20 nA beam current with a 20-micron beam size. Data for Si, Al, Ca, Na, K and Fe were analyzed using plagioclase and iron oxide standards (*Supplementary Table*).

The TEM samples were prepared by crushing small plagioclase grains selected from area close to the points analyzed by EMPA in ethanol with an agate mortar. Drops of the suspension were placed on lacey-carbon coated Cu grids, and the small flaky crystals are left on the Cu grid after the ethanol evaporates. TEM images and selected-area electron diffraction pattern (SAED) were taken using a Philips CM200UT TEM. Compositions of the samples were examined by attached X-ray energy-dispersive spectroscopy (EDS). The EDS results are calibrated with the results from electron microprobe analyses.

The crystals for single crystal X-ray diffraction were picked after microprobe analyses. Areas with composition around An_{50-52} were selected. Crystals are washed with acetone to clean off the crystalbond from the thin section and any attached small grains, and then mounted on glass fibers with epoxy glue. The X-ray diffraction data were collected on a Bruker Quazar APEXII single crystal diffractometer with Mo Kα IμS source at 100K. 4 ω runs and 1 φ run were programmed for each sample with a scan width of 0.5°. Exposure times of 65s, 95s, and 65s were applied for Dul-15-8B, SK90-12 and R2923 respectively. The instrument was running at power of 50kV and

0.6mA. The detector was at a distance of 5cm from the crystal. The X-ray diffraction data for sample Dul-15-8B was analyzed again on a Bruker D8 VENTURE X-ray diffractometer, equipped with an air-cooled PHOTON II detector using CMOS technology. The X-ray source was an Incoatec Mo IμS 3.0 microfocus tube coupled to a multilayer mirror optic. Data were collected at 100K using an Oxford Cryosystems Cryostream 800 low-temperature apparatus to intensify high-angle satellites. This new instrument is applied specifically for sample Dul-15-8B sample to confirm the nonexistence of *f*-reflections (second order satellites). More experimental details are provided in *Table 1*.

Unit cell parameters were calculated and refined using APEX3 software. The structure was solved with a charge-flipping algorithm (Oszlanyi and Suto, 2004, 2005) using SUPERFLIP (Palatinus and Chapuis, 2007). The refinement of the average structure and modulated structure was done with JANA2006 (Petříček *et al.*, 2014). The 3-D crystal structure was visualized by VESTA (Momma and Izumi, 2011).

Structure Refinement

Sample Dul-15-8B

After the data were collected on Bruker Quazar APEXII with 65s exposure time, no *f*-reflections were observed. To confirm the extinction of second order satellites, the same crystal was analyzed again on a Bruker D8 VENTURE diffractometer for 90s exposure. With much stronger beam intensity, a more sensitive detector and longer exposure time, still no *f*-reflections were detected. Thus, the second-order satellites were confirmed to be absent. Therefore, no second order component should be allowed in the modulation function.

The modulated structure of Dul-15-8B was refined in the unconventional $X\bar{1}(\alpha\beta\gamma)0$ superspace group setting, with c~14Å subcell and a centering condition of (½ ½ ½ 0), (0 0 ½ ½), (½ ½ 0 ½) (Boysen and Kek, 2015; Jin and Xu, 2017). Symbol (αβγ) indicates the modulation is not constrained by the symmetry of the structure thus should have components along all three unit cell axes (***q***-vector in *Table 1*). The model used for refinement is the same as the metamorphic labradorite (987L) refinement by Jin and Xu (2017), with M2 only occupied by Ca and M1 containing both Ca and Na. The potassium component is not considered in the refinement. The

198 total occupancy of the atoms in M1 and M2 sites are constrained to 1. Since no second-order
199 satellites were observed, all atomic modulation functions are described by simple harmonic
200 functions, including the atomic displacement parameters (ADPs or temperature parameters). The
201 resulting atomic occupancies and positions are listed in *Table 2*. Detailed information about the
202 crystal can be found in *Supplementary Data*.

203 The Al occupancies of tetrahedral sites are assigned according to the <T-O> bond distances (Å),
204 following the equation (Kroll and Ribbe, 1983):

$$\mathrm{Occ(Al)} = 0.25(1 + \mathrm{n_{An}}) + (< \mathrm{T_i} - \mathrm{O} > - \ll \mathrm{T} - \mathrm{O} \gg)/k$$

205 The value of k is estimated to be 0.135Å, which is conventionally used for albite and plagioclase
206 feldspars (Angel *et al.*, 1990; Jin and Xu, 2017). The resulting occupancies of all tetrahedral sites
207 lie in the reasonable range (between 0 and 1). The modulation of <T-O> bond distances is
208 plotted in Fig. 4**A**. The average <T-O> bond distances for T_1o, T_1m, T_2o and T_2m are 1.6852Å,
209 1.6555Å, 1.6527Å and 1.6581Å, corresponding to Al occupancies of 0.55, 0.33, 0.31 and 0.35
210 respectively.

211 The displacement modulation of the M site shows a similar pattern as the structure of the
212 metamorphic labradorite sample (987L), with the M2 site (Ca) almost stationary and the M1 site
213 (Ca+Na) moving back and forth (Jin and Xu, 2017). The displacement happens mainly within the
214 ***b*-*c*** plane as the component along ***a***-axis is very minor (Fig. 5**A**). The amplitude of M1
215 displacement, however, is obviously smaller compared to the structure of sample 987L (Jin and
216 Xu, 2017). The occupational modulation of M site is not as dramatic as in the metamorphic
217 labradorite structure (Jin and Xu, 2017), as shown in Fig. 6**A**. The variation (max-min in Table 2)
218 of occupational modulation of Na in M1 site is 0.07, whereas in 987L the maximum difference in
219 Na occupancy is 0.35.

220 As explained by Jin and Xu (2017), the structure with no second-order satellites (*f*-reflections)
221 would not display a density modulation. As shown in Fig. 7**A**, where all Na occupancies of all 8
222 symmetrically equivalent M sites are plotted, the average occupancy shows a virtually constant
223 value. Therefore, the structure is chemically homogenous with only ordering within each subcell.
224 For comparison, the average <T-O> bond distances are also plotted in Fig. 8**A**. Even though the
225 individual average distance shows some variation (less than 0.005), the overall average bond

distance of all the T-sites, which corresponds to the chemical composition (Kroll and Ribbe, 1983), is basically constant.

A section of the modulated structure consisting of 3x7 anorthite unit cells along ***b***- and ***c***-axis is presented in Fig. 9. The structure can still be described as periodic domains with polarity related by $I\bar{1}$ inversion twin boundaries, except the inversion boundaries have the same composition as the *I*1-like domains. The ordering of Si-Al at inversion twin boundaries shows an anorthite-like pattern, with Al-rich sites surrounded by 4 Si-rich sites and vice versa. The ordering pattern of the *I*1-like domains is unique and different from albite and anorthite structures. The Al occupancy of T_1o sites in the *I*1-like domains is not higher than in the inversion twin boundaries, whereas in low-temperature labradorite structure (Jin and Xu, 2017), the T_1o site in the *I*1-like domains (rich in Na) is higher than the inversion twin boundaries, even though the total Al component is lower than that at the inversion twin boundaries.

The M site configuration is always complicated in plagioclase structure. The correlation between the split distance of M site and the surrounding tetrahedral framework was observed in the low temperature labradorite structure (Jin and Xu, 2017). As shown in Fig. 10, the M site lies almost exactly on the plane defined by the T_2 sites. The split direction of the M site is very close to the diagonal line connecting T_2 sites. The split distance of M site is plotted against the diagonal distance between T_2oz and T_2mo and shown in Fig. 11**A**. The two values are correlated with each other, as the M site is more split where the diagonal T_2 distance is larger. The modulation function of T_1o-O_A1-T_1m angle is provided in Fig. 12**A**. The two angles are tilting towards opposite (inward vs outward), except for when t=0 and t=0.5.

Sample SK90-12

With 95 seconds of exposure time, 284 *f*-reflections were observed in the X-ray diffraction data of Sample SK90-12, which is fewer than the number observed in low-temperature labradorite (sample 987L, 60s exposure) (Jin and Xu, 2017). The structure of Sample SK90-12 is refined in exactly the same model as sample 987L (Jin and Xu, 2017) with the same constrains. Therefore, all parameters are refined with a sum of harmonic functions of first and second order. The result

255 atomic occupancies and positions are listed in *Table 3*. Complete structural information can be
256 found in *Supplementary Data*.

257 The M site modulation shows very similar pattern to the Dul-15-8B sample, but with an obvious
258 tendency towards the more ordered structure as low-temperature labradorite (Fig. 5**B**) (Jin and
259 Xu, 2017). The modulation of Na in the structure, modified by the second-order component of
260 the modulation function, shows two separate and definite maxima within one period (Fig. 6**B**).
261 Although the variation of the occupancy modulation is only slightly larger than that in sample
262 Dul-15-8B and much smaller than that in the low-temperature labradorite (Jin and Xu, 2017). By
263 averaging all 8 symmetrically equivalent Na occupancies within one unit cell (c~14Å), a density
264 modulation with variation of ~8 mole % of anorthite is displayed (Fig. 7**B**).

265 The <T-O> bond distance modulation pattern also lies somewhere between sample Dul-15-8B
266 and the low-temperature labradorite (987L) (Fig. 4**B**). The average <T-O> bond distances for
267 T_1o, T_1m, T_2o and T_2m are 1.6876Å, 1.6547Å, 1.6504Å and 1.6575Å, corresponding to Al
268 occupancies of 0.56, 0.32, 0.29 and 0.34 respectively. The modulated bond distance function of
269 $<T_1o\text{-}O>$ and $<T_1m\text{-}O>$ is starting to broaden between t=0.25 and t=0.5. The variation of bond
270 distance modulation is also bigger than that of Dul-15-8B. The $<T_1o\text{-}O>$ bond, for example, has
271 a variation of ~0.1Å between the maximum and minimum values, whereas the variations in Dul-
272 15-8B and low-temperature labradorite (987L) are ~0.08Å and ~0.12Å respectively (Jin and Xu,
273 2017). The difference is even more obvious when we average all the symmetrically equivalent
274 sites within one unit cell (Fig. 8**B**). The average $<T_2\text{-}O>$ distances and the overall average
275 obviously show two maxima and two minima in one modulation period. The averages resemble
276 the pattern in the low-temperature labradorite sample 987L (Jin and Xu, 2017) but are different
277 from the pattern in sample Dul-15-8B. The correlation between the split distance of M site and
278 the diagonal distance of T_2 sites are shown in Fig. 11**B**. Both the variation of the M1-M2
279 distance and the diagonal T_2 distance are larger than in Dul-15-8B. The modulation of bond
280 angles also shows larger amplitude as plotted in Fig. 12.

281

282

283

Sample R2923

Iridescent color in labradorite feldspars are generated by nanoscale semiperiodic exsolution lamellae within the crystal. The thickness, or period of the lamellae is at the same scale with the wavelength of visible light. Therefore, light of certain color/wavelength would be reflected by the exsolution lamellae boundaries and interfere with each other, and display beautiful iridescent colors. Thicker exsolution lamellae would generate iridescent color with longer wavelength. Almost all previous labradorite samples used for single crystal X-ray analyses display blue iridescent color (Horst *et al.*, 1981; Yamamoto *et al.*, 1984; Boysen and Kek, 2015). This was considered a serious problem (Ribbe, 1983a), as the reflections from the two components overlap and therefore any structure refined is a composite of two structures of different compositions. The difference of the *e*-fringes across the exsolution lamellae is measured to be at least 10 degrees in a sample with blue iridescent color (McConnell, 1974; Wenk and Nakajima, 1980; Ribbe, 1983a). However, all igneous labradorite within the range of Bøggild intergrowth that are cooled extremely slowly would display exsolution lamellae. Therefore, the structure of sample R2923 was refined as a single phase, simply for the purpose of comparison.

As observed with TEM (Fig. 2), even though the exsolution lamellae are clearly seen, the difference of *e*-fringes across the exsolution lamellae is very minor, indicating a minor difference in composition and structure between the two phases. And the structure is dominated by the Ca-rich phase, unlike the sample with blue iridescent color where the two phases are almost of the same proportion. Therefore, the labradorite with red iridescent color should be a better subject for single crystal diffraction, and the refinement result should be more reliable than that of a sample with blue iridescent color. With an R value of 0.07 for *f*-reflections (second-order satellites) and 0.03 for all reflections, the degree of fit of this refinement exceeds all previous iridescent labradorite structures, which suggests that the resulting structure should be a good approximation of both exsolution lamellae.

There were less than 300 third-order satellites observed during the data collection (Fig. S1 in Supplementary Material). This is very likely to have resulted from the suppressed thermal vibration and enhanced intensities by low temperature data collection. But considering they are weak and not from a pure phase, and also for the convenience of comparison, the third order satellites were not used in the refinement. The structure was refined in the same model with the

same conditions as the low-temperature labradorite sample (987L), except only the first-order harmonic wave was used for the atomic displacement parameters (ADPs or temperature parameters) modulation to avoid unrealistic results. The chemical composition based on the refined M site occupancies is about An_{49}, which is obviously lower than the microprobe analysis result. This disagreement is hardly surprising as the reflections used for refinement are simply a sum integration of overlapped reflections from two different lamellae phases. Nonetheless, to get a better idea of the structure, we constrained the total occupancy of Ca in M site to be 0.525 based on the microprobe analyses (*Supplementary Table*). The atomic occupancies and positions are listed in *Table 4*. Complete information of the modulated structure can be found in *Supplementary Data*.

The resulting structure of R2923 is very similar to the low-temperature labradorite (sample 987L) (Jin and Xu, 2017). The modulation orientations and periods of the two samples are basically the same. The modulation of M site also matches that in the metamorphic labradorite (sample 987L) (Jin and Xu, 2017) very well. Both the occupancy (Fig. 6**C**) and displacement (Fig. 5**C**) modulation are very similar to the modulation in sample 987L, even the electron density contour (Fig. 5**C**) matches with 987L surprisingly well. And by averaging all 8 symmetrically equivalent Na occupancies within one unit cell (c~14Å), a density modulation with variation of ~17 mole% of anorthite is displayed (Fig. 7**C**).

The <T-O> bond distance modulation is also indistinguishable from the 987L sample (Fig. 4**C** and Fig. 8**C**) (Jin and Xu, 2017). The modulation functions are obviously flattened in certain part of the modulation period (Fig. 4**C**), which distinctly distinguish the structure from sample Dul-15-8B. Based on the same function, the average <T-O> bond distances for T_1o, T_1m, T_2o and T_2m are 1.6935Å, 1.6516Å, 1.6508Å and 1.6571Å, corresponding to Al occupancies of 0.61, 0.29,0.29 and 0.34 respectively. The correlation between M site split distance and diagonal T_2 distance displays an elongated loop compare to that of Dul-15-8B and SK90-12 (Fig. 11**C**). The modulation of T_1o-O_A1-T_1m angle also shows larger amplitude compared to Dul-15-8B and SK90-12 Fig. 12**C**.

Discussion

The *e*-plagioclase feldspars were previously divided into two categories based on the existence of *f*-reflections, namely *e*1 and *e*2 (Ribbe, 1983b; Smith and Brown, 1988; Carpenter, 1994). The compositional difference was believed to be the reason causing this difference, as *f*-reflections barely appear in Na-rich *e*-plagioclase but are very common in Ca-rich *e*-plagioclase (Bown and Gay, 1959; Smith and Brown, 1988). Many previous refinements of the structure only considered first-order satellites (*e*-reflections) and neglected the weak *f*-reflections (Horst *et al.*, 1981; Yamamoto *et al.*, 1984), and thus failed to resolve any difference between *e*1 and *e*2 structures. The discovery of *f*-reflections in a Na-rich plagioclase (~An_{45}) raised the complexity of the case, and revealed cooling rate as an important factor in addition to composition in determining the structure of *e*-plagioclase (Xu *et al.*, 2016). Because the satellites in Na-rich plagioclase samples are usually weak, which makes data collection and structure refinement very difficult, only one *e*2 structure (An38) refinement has been previously published (Steurer and Jagodzinski, 1988). Nonetheless, since there is no evidence suggesting otherwise, we are categorizing the structure of sample Dul-15-8B as *e*2, which is the same as most Na-rich *e*-plagioclase feldspars.

With a sufficiently long X-ray beam exposure time for sample Dul-15-8B, we can confirm the extinction of second order satellites (*f*-reflections) and the absence of density modulation, which means the difference between *e*1 and *e*2 is distinct and they should be categorized as two separate modulated structures. On the other hand, the structure refinement does show great similarities between two phases, which made the differences hard to uncover when *f*-reflections were neglected. Other than the absence of density modulation, there are a few noticeable differences in the *e*2 structure from *e*1. The amplitudes of the modulated parameters are systemically smaller than those of the *e*1 structure. For instance, the $<T_1o\text{-}O>$ bond distance modulation of sample Dul-15-8B dropped nearly 30% in variation from the iridescent labradorite (sample R2923). The average occupancies in tetrahedral sites are also different. Average Al occupancy in T_1o site is 0.55 for sample Dul-15-8B, which is obviously smaller than 0.59 in low-temperature labradorite (sample 987L) (Jin and Xu, 2017) and 0.61 in the iridescent labradorite (sample R2923).

372 The modulation period is another important difference between *e*1 and *e*2 structures. With very
373 similar chemical composition, the modulation period of sample Dul-15-8B is ~34Å, which is
374 about 4Å longer than that of the iridescent labradorite sample R2923 and low-temperature
375 labradorite (sample 987L) (Jin and Xu, 2017). This result confirms the discontinuity observed by
376 Slimming (1976) in electron diffraction patterns of *e*-plagioclase feldspars with different
377 compositions. The orientation of the modulation is also different from more ordered *e*-
378 plagioclase (*e*1), tilting towards the Ca-rich side on the trend (Fig. 13).

379 It is worth noting that even though sample SK90-12 starts to show weak *f*-reflections, the
380 modulation period and orientation are still close to sample Dul-15-8B (Fig. 13). This indicates
381 the crystal was transformed from *e*2 into *e*1 phase, where density modulation is starting to form
382 on the foundation of the *e*2 modulation period and orientation. Carpenter plotted the modulation
383 period against the composition for igneous samples from Skaergaard and metamorphic samples
384 from Broken Hill (Figure 15 in Carpenter, 1994), based on data from Gay (1956) and Slimming
385 (1976). The metamorphic samples show a discontinuous trend whereas the igneous samples
386 show a continuous one. As the SK90-12 sample in this study shows no evidence of exsolution,
387 the divergence of the trends can be easily explained by the different trend of *e*1 and *e*2, instead of
388 introduced by Bøggild intergrowth. While the Skaergaard sample may start to develop *e*1
389 ordering from *e*2 structure, it still preserves the modulation period and orientation of *e*2. As
390 Carpenter (1994) proposed, once a given structure is established (*e*2 in this case), the energy
391 advantage of reorientation will probably be small compared to degree of structural reorganization
392 required. The metamorphic Ca-rich plagioclase samples, on the other hand, formed directly at the
393 temperature where *e*1 structure is stable, therefore the modulation period and orientation follows
394 a different trend from *e*2. So the data points in Figure 15 of Carpenter (1994) should follow two
395 separate trends: where all the Skaergaard samples and Na-rich metamorphic samples follow the
396 nice *e*2 trend, and the Ca-rich metamorphic samples follow the *e*1 trend.

397 With the structure of *e*-plagioclase solved, there is no reason to still think that *e*-plagioclase is a
398 metastable stage leading to an unmixing of the structure into albite and anorthite. First of all, the
399 modulation period does not get longer as the cooling rate of *e*-plagioclase decreases, whereas in
400 exsolution process, the exsolution lamellae tends to grow thicker through time; the modulation
401 period of *e*-plagioclase gets longer as the Ca component of the composition increases, which also

distinguish the ordering of *e*-plagioclase from an unmixing process; and finally, spinodal decomposition is a non-equilibrium process, and should produce a relatively randomly distributed wavelength, instead of the perfectly ordered structure with strictly constrained period and orientation we see in *e*-plagioclase structure. Therefore, there is no doubt that *e*-plagioclase structures are thermodynamically stable for intermediate plagioclase at low temperature.

All the parameters used to estimate the ordering state of intermediate plagioclase were based on the average structure, such as <T_1o-O> bond distance, gamma angle of the lattice parameters (Kroll, 1983; Smith and Brown, 1988). Although Al occupancy in T_1o site can indicate ordering sates of alkali feldspars, it does not work well for intermediate plagioclase like labradorite feldspars based on their average structures. Intermediate plagioclase feldspars display structural modulation that characterized by additional *e*- and *f*-reflections. As the three samples refined in this paper clearly show an increasing ordering state, and the structures are described in great detail, we should be able to extract some more accurate parameters to quantify the ordering states of the plagioclase structures. Some potential parameters are listed in *Table 5*. Variation of Na occupancy, variation of density modulation, and variation of <T_1o-O> bond distance modulation of the three samples are plotted against the gamma angles in Fig. 14, where clear correlations between the parameters are shown. The gamma angle is a simple way for qualifying the ordering state of intermediate plagioclase feldspar. However, it cannot tell any detailed ordering state within the structure, let alone the difference among *e*1, *e*2 and $C\bar{1}$. The structural modulation on the other hand, shows relatively large variation among different ordering states, and clearly shows the difference among the three labradorite feldspar phases. The calorimetry work by Carpenter *et al* (1985) reveals the significant enthalpy change associated with the ordering of *e*-plagioclase. The enthalpy difference between a disordered plagioclase with $C\bar{1}$ symmetry and a highly ordered *e*-plagioclase can be up to ~3 kcal/mole. The ordering states of the samples used in their paper were only qualitatively characterized by the intensity and sharpness of the satellite reflections in the electron diffraction pattern, which are very difficult to compare with one another due to the difference in thickness and orientation of the TEM sample. However, with single crystal diffraction data, the ordering enthalpy and the modulated structure could be directly connected, leading us to a comprehensive and detailed picture of the thermodynamics of plagioclase feldspar solid solution.

The discovery of an *e*2 structure with Ca-rich composition (~An_{52}) raises another problem that needs to be solved, as *e*2 structure does not appear at this composition in any previously proposed phase diagrams. It was reported that disordered $C\bar{1}$ structure is stable at high temperature for this composition (Smith and Brown, 1988; Carpenter, 1994), and homogenous *e*1 structure is stable at low temperature (below ~550℃) (McConnell, 2008; Jin and Xu, 2017).

Disordered $C\bar{1}$ structure transforms to *e*2 structure on the Na-rich side of Bøggild intergrowth (Carpenter, 1994; McConnell, 2008). Therefore, the solvus for Bøggild intergrowth must be shaped as a loop which closes at low temperature, and serves as a first-order phase transition boundary between disordered $C\bar{1}$ structure and *e*1 structure (McConnell, 2008; Jin and Xu, 2017; Xu *et al.*, 2016). In this scenario, *e*2 cannot be a stable phase at any temperature for this composition, but is more likely to be a metastable phase that is kinetically preferable when exsolution is suppressed. Exsolution requires interdiffusion between CaAl and NaSi, which is extremely sluggish (Grove *et al.*, 1984; Liu and Yund, 1992). A schematic diagram showing the topology of these phases is provided in Fig. 15. The phase boundary between disordered $C\bar{1}$ structure and *e*2 is extended as the dash line. A corresponding time-temperature-transformation (TTT) diagram for plagioclase of ~An_{51} composition is also illustrated in Fig. 16. If the crystal is quenched from high temperature (an erupted volcanic rock, for instance), the disordered $C\bar{1}$ structure, which is stable only at high temperature, would be preserved (path **A** in Fig. 16). In a quickly cooled host rock (as in sample Dul-15-8B), a disordered $C\bar{1}$ structure will not exsolve into *e*1 structure, but transforms to *e*2 instead (path **B** in Fig. 16). As the cooling process gets slower (path **C** in Fig. 16), the *e*2 structure will end up supercooled in the area where *e*1 is stable, and further ordering results in *e*1 structure while the *e*2 modulation period and orientation is still preserved (as in sample SK90-12). As for an extremely slow-cooled sample (sample R2923), exsolution would take over once it enters the two-phase area of $C\bar{1}$ structure and *e*1 and form Bøggild intergrowth (path **D** in Fig. 16). When the temperature gets below the loop solvus, the Ca-poor lamellae would also transform from $C\bar{1}$ structure to *e*1, and the crystal will try to homogenize into one single *e*1 phase. However, the temperature then would be too low for the process to go to completion, therefore the exsolution lamellae are preserved.

Carpenter (1986) observed *e* ordering above the reversed $e \rightleftharpoons I\bar{1}$ transition with starting crystals of $C\bar{1}$ structure. The structure will transform eventually to $I\bar{1}$ structure if held long enough at the

same temperature. This was explained, reasonably, as a metastable structure appearing in the stable field of $I\bar{1}$ structure, but the metastable *e* structure was presumed to be *e*1 based on the composition in his paper. However, since ordering of *e*1 structure requires atom exchange outside a unit cell, it is unlikely that *e*1 is kinetically preferable to $I\bar{1}$ structure. The big miscibility gap between $C\bar{1}$ and *e*1 phase also supports this, while no gap has been observed between $C\bar{1}$ and $I\bar{1}$ (Carpenter and McConnell, 1984). By comparing the structure of $C\bar{1}$, *e*2 and $I\bar{1}$, it is obvious that the *e*2 structure is actually closer to $C\bar{1}$ structure. Both $C\bar{1}$ and *e*2 structure are chemically homogenous without density modulation; transition from $C\bar{1}$ to *e*2 only requires total reordering of tetrahedral sites of the inversion twin boundaries and minor adjustment for the *I*1-like domains, whereas $I\bar{1}$ requires reordering of tetrahedral sites of every $C\bar{1}$ unit cell throughout the crystal. The T site bond distance modulations in sample Dul-15-8B show a considerable extent of ordering. However, the transition from $C\bar{1}$ to *e*2 might be initiated by only M site ordering, as the volcanic plagioclase sample from Hogarth Ranges already starts to show weak *e*-reflections (Fitz Gerald et al. 1986). Therefore, *e*2 structure is very likely to be more kinetically favorable than $I\bar{1}$ structure for a starting crystal with $C\bar{1}$ structure at certain temperature. As shown in Fig. 15, the extended boundary between $C\bar{1}$ and *e*2 might be above the boundary between $I\bar{1}$ and *e*1. Nonetheless, it would require careful measurement of the modulation period and orientation of the experiment product in Carpenter's (1986) paper to confirm this theory.

Implications

The single crystal X-Ray analyses of *e*1 and *e*2 structures with similar compositions reveals the complicated phase relations around Bøggild intergrowth. The *e*2 structure is confirmed to be a distinctly different phase from *e*1, but the two modulated structures are similar in many ways. The *e*2 structure is characterized by the absence of second-order satellites (*f*-reflections), indicating a less ordered state compared to the *e*1 structure. It can also be described as periodic *I*1-like domains related by $I\bar{1}$ like inversion boundaries. However, with no density modulation, the domains are of the same chemical composition as the inversion twin boundaries. The variations of modulated parameters in *e*2 structure are systematically smaller than *e*1 structure.

The average Al occupancy in T_1o site of *e*2 structure is smaller compared to *e*1 structure for the same composition, and the modulation period is longer than in the *e*1 structure.

The structure of *e*2 is closer to $C\bar{1}$ structure, for only the tetrahedral sites of inversion boundaries need to be completely rearranged. This similarity makes it kinetically preferable for a crystal cooled from a $C\bar{1}$ structure. The *e*2 phase normally exists as a stable phase for Na-rich plagioclase at a relatively low temperature. Nevertheless, it can also appear as a metastable phase for Ca-rich plagioclase, as the energy barrier for the phase transition from $C\bar{1}$ to *e*1 or even $I\bar{1}$ can be relatively big. A fast-cooled plagioclase feldspar (~An_{51}) will not exsolve, but transforms into the *e*2 structure instead. The supercooled *e*2 structure would eventually transform to *e*1 if a long enough cooling time is allowed, but with the modulation period and orientation of *e*2 preserved. Only extremely slowly cooled plagioclase would exsolve to *e*1 directly and follow the same modulation period and orientation as in metamorphic rock.

The result of this research clears up the topology of the lower end of the solvus loop for Bøggild intergrowth. The case for the higher end of the loop could be more complicated. Meanwhile, the nature and exact position of the boundary between *e*1 and *e*2 are still not clear. The two structures behave differently, but the symmetry did not change at all from this phase transition. Further work needs to be done for plagioclase samples with various cooling history on both sides of the Bøggild miscibility gap to comprehend the phase relations between $C\bar{1}$, $I\bar{1}$, *e*1 and *e*2.

The completed structure variations of plagioclase could also be employed to develop a geospeedometry for quantifying the cooling rates of igneous rocks (Fig. 16). The new parameters such as amplitudes of modulation waves, are proved to be much more sensitive and accurate in quantifying the ordering states of intermediate plagioclase structures, compared to the conventionally used gamma angles or T_1o occupancies of the average structure. These parameters could be calibrated either internally, based on the CaAl-NaSi interdiffusion rates in plagioclase from experiment data, or externally using cooling rate of the same rock calculated by other methods.

Acknowledgements

519 This study was supported by NSF (EAR-1530614) and the NASA Astrobiology Institute (N07-
520 5489). Authors thank Professor Adriana Heimann-Rios for providing us the Skaergaard sample,
521 Dr. Bruce Noll of Bruker AXS for allowing us to use Bruker D8 VENTURE X-ray
522 diffractometer, Dr. Mario Tribaudino, Mr. Franklin Hobbs, and an anonymous reviewer for and
523 providing helpful comments and suggestions.

524

525

References

Angel, R.J., Carpenter, M.A. and Finger, L.W. (1990) Structural variation associated with compositional variation and order-disorder behavior in anorthite-rich feldspars. American Mineralogist 75(1-2), 150-162.

Bown, M.G. and Gay, P. (1959) The reciprocal lattice geometry of the plagioclase felspar structures. Zeitschrift für Kristallographie 111(1-6), 1-14.

Boysen, H. and Kek, S. (2015) The modulated structure of labradorite. Zeitschrift für Kristallographie 230(1), 23-36.

Carpenter, M.A. (1986) Experimental delineation of the $e \rightleftharpoons I\bar{1}$ and $e \rightleftharpoons C\bar{1}$ transformations in intermediate plagioclase feldspars. Physics and Chemistry of Minerals 13(2), 119-139.

Carpenter, M.A. (1994) Subsolidus phase-relations of the plagioclase feldspar solid-solution. Pp. 221-269. In I. Parsons, Ed. *Feldspars and their reactions*, Vol, 421, Kluwer Academic Publishers, Dordrecht.

Carpenter, M.A. and McConnell, J.D.C. (1984) Experimental delineation of the $C\bar{1} \rightleftharpoons I\bar{1}$ transformation in intermediate plagioclase feldspars. American Mineralogist 69(1-2), 112-121.

Carpenter, M.A., McConnell, J.D.C. and Navrotsky, A. (1985) Enthalpies of ordering in the plagioclase feldspar solid-solution. Geochimica et Cosmochimica Acta 49(4), 947-966.

Chao, S.H. and Taylor, W.H. (1940) Isomorphous replacement and superlattice structures in the plagioclase feldspars, pp. 76-87.

Fitz Gerald, J.D., Parise, J.B. and Mackinnon, I.D.R. (1986) Average structure of an An_{48} plagioclase from the Hogarth Ranges. American Mineralogist 71(11-12), 1399-1408.

Gay, P. (1956) The structures of the plagioclase feldspars: VI. Natural intermediate plagioclases. Mineralogical Magazine 31(232), 21-40.

Grove, T.L., Baker, M.B. and Kinzler, R.J. (1984) Coupled CaAl-NaSi diffusion in plagioclase feldspar: experiments and applications to cooling rate speedometry. Geochimica et Cosmochimica Acta 48(10), 2113-2121.

553 Horst, W., Tagai, T., Korekawa, M. and Jagodzinski, H. (1981) Modulated structure of a
554 plagioclase An_{52}: Theory and structure determination, p. 233.

555 Janssen, T., Chapuis, G. and De Boissieu, M. (2007) Aperiodic crystals: from modulated phases
556 to quasicrystals, Oxford University Press, New York.

557 Jin, S. and Xu, H. (2017) Solved: The enigma of labradorite feldspar with incommensurately
558 modulated structure. American Mineralogist 102(1), 21-32.

559 Kroll, H. (1983) Lattice parameters and determinative methods for plagioclase and ternary
560 feldspars. Pp. 101-119. In P.H. Ribbe, Ed. Feldspar mineralogy, 2nd ed., Vol. 2, Reviews
561 in Mineralogy, Mineralogical Society of American, Washington, D.C.

562 Kroll, H. and Ribbe, P.H. (1983) Lattice parameters, composition and Al, Si order in alkali
563 feldspars. Pp. 57-100. In P.H. Ribbe, Ed. Feldspar mineralogy, 2nd ed., Vol. 2, Reviews
564 in Mineralogy, Mineralogical Society of American, Washington, D.C.

565 Liu, M. and Yund, R.A. (1992) NaSi-CaAl interdiffusion in plagioclase. American Mineralogist
566 77(3-4), 275-283.

567 McConnell, J.D.C. (1974) Analysis of the time-temperature-transformation behaviour of the
568 plagioclase feldspars. Pp. 460-477. The feldspars, Manchester University Press, New
569 York.

570 McConnell, J.D.C. (2008) The origin and characteristics of the incommensurate structures in the
571 plagioclase feldspars. The Canadian Mineralogist 46(6), 1389-1400.

572 Momma, K. and Izumi, F. (2011) VESTA 3 for three-dimensional visualization of crystal,
573 volumetric and morphology data. Journal of Applied Crystallography 44(6), 1272-1276.

574 Nielsen, T.F.D. (2004) The shape and volume of the Skaergaard intrusion, Greenland:
575 Implications for mass balance and bulk composition. Journal of Petrology 45(3), 507-530.

576 Oszlanyi, G. and Suto, A. (2004) Ab initio structure solution by charge flipping. Acta
577 Crystallographica Section A 60(2), 134-141.

578 Oszlanyi, G. and Suto, A. (2005) Ab initio structure solution by charge flipping. II. Use of weak
579 reflections. Acta Crystallographica Section A 61(1), 147-152.

580 Palatinus, L. and Chapuis, G. (2007) SUPERFLIP - a computer program for the solution of
581 crystal structures by charge flipping in arbitrary dimensions. Journal of Applied
582 Crystallography 40(4), 786-790.

583 Petříček, V., Dušek, M. and Palatinus, L. (2014) Crystallographic Computing System JANA2006:
584 General features. Zeitschrift für Kristallographie 229(5), 345.

585 Ribbe, P.H. (1983a) Aluminum-silicon order in feldspars: Domain textures and diffraction. Pp.
586 21-56. In P.H. Ribbe, Ed. Feldspar mineralogy, 2nd ed., Vol. 2, Reviews in Mineralogy,
587 Mineralogical Society of American, Washington, D.C.

588 Ribbe, P.H. (1983b) Exsolution textures in ternary and plagioclase feldspars; interference colors.
589 Pp. 241-270. In P.H. Ribbe, Ed. Feldspar mineralogy, 2nd ed., Vol. 2, Reviews in
590 Mineralogy, Mineralogical Society of American, Washington, D.C.

591 Slimming, E.H. (1976) An electron diffraction study of some intermediate plagioclases.
592 American Mineralogist 61(1-2), 54-59.

593 Smith, J.V. (1984) Phase relations of plagioclase feldspars. Pp. 55-94. In W.L. Brown, Ed.
594 Feldspars and feldspathoids, Vol. 137, Reidel Publishing Company, Dordrecht.

595 Smith, J.V. and Brown, W.L. (1988) Feldspar Minerals, Springer-Verlag, Berlin Heidelberg.

596 Steurer, W. and Jagodzinski, H. (1988) The incommensurately modulated structure of an
597 andesine (An38). Acta Crystallographica Section B 44(4), 344-351.

598 Taylor, R.B. (1964) Geology of the Duluth Gabbro Complex near Duluth, Minnesota. Minnesota
599 Geological Survey (Bulletin No. 44), 1-63.

600 Toplis, M.J., Brown, W.L. and Pupier, E. (2008) Plagioclase in the Skaergaard intrusion. Part 1:
601 Core and rim compositions in the layered series. Contributions to Mineralogy and
602 Petrology 155(3), 329-340.

603 van Smaalen, S. (2007) Incommensurate crystallography, Oxford University Press, USA, New
604 York.

Wagner, T. and Schoenleber, A. (2009) A non-mathematical introduction to the superspace description of modulated structures. Acta Crystallographica Section B: Structural Science 65(3), 249-268.

Wenk, H.-R. and Nakajima, Y. (1980) Structure, formation, and decomposition of APB's in calcic plagioclase. Physics and Chemistry of Minerals 186.

Winter, J.D. (2010) An introduction to igneous and metamorphic petrology, Prentice Hall, New Jersey.

Xu, H. (2015) Direct observation of Ca-Na ordering and structure polarity in Ca-rich intermediate plagioclase feldspar with incommensurate modulated structure. American Mineralogist 100(2-3), 510-515.

Xu, H., Jin, S. and Noll, B.C. (2016) Incommensurate density modulation in a Na-rich plagioclase feldspar: Z-contrast imaging and single-crystal X-ray diffraction study. Acta Crystallographica Section B 72(6), 904-915.

Yamamoto, A., Nakazawa, H., Kitamura, M. and Morimoto, N. (1984) The Modulated Structure of Intermediate Plagioclase Feldspar $Ca_xNa_{1-x}Al_{1+x}Si_{3-x}O_8$. Acta Crystallographica Section B 40(Jun), 228-237.

Captions of Figures

Fig. 1 Dark-field image (left) and selected-area electron diffraction (SAED) pattern ([111] zone-axis) of sample Dul-15-8B. The SAED pattern (right) shows weak and diffuse *e*-reflections and no *f*-reflections.

Fig. 2 Dark-field image and SAED pattern of sample SK90-12. The image (left) shows homogenous *e*-fringes with no exsolution lamellae. The diffraction pattern (right) ($[5\bar{1}1]$ zone axis) shows sharp *e*-reflections and weak *f*-reflections next to main reflections (indexed). A fast Fourier transform (FFT) pattern is inserted at the left of the TEM image.

Fig. 3 **A.** Bright-field TEM image of sample R2923 showing nearly periodic exsolution lamellae. The wide lamellae (~230 nm thick) are Ca-rich. **B.** SAED pattern ($[5\bar{1}1]$ zone axis) of R2923, showing strong *e*- and *f*-reflections, some weak third order satellite reflections can also be observed. **C.** Dark-field TEM image showing e-fringes crossing the exsolution lamellae boundary, with a slight change in orientation (~2 degrees or less) and period. The difference in *e*-reflections of different lamellae is indistinguishable in the diffraction pattern.

Fig. 4 <T-O> bond distances of individual tetrahedral sites for the three samples. **A.** Sample Dul-15-8B; **B.** Sample SK90-12; **C.** Sample R2923. The modulation function wave shows flat part (e.g. T_1m between t=0.2 and t=0.5; T_2m between t=0.9 and t=0.2).

Fig. 5 The displacement modulation along three axes and electron density contour variation for all three samples, the red line represents M2(Ca) and green line represents M1(Na+Ca), xi (i = 1, 2, 3, 4) are unit cell edge in (3+1)D space. **A.** Sample Dul-15-8B; **B.** Sample SK90-12; **C.** Sample R2923.

Fig. 6 Ca/Na occupancy modulation of M1(Ca+Na) and M2(Ca) site of three samples. **A.** Sample Dul-15-8B; **B.** Sample SK90-12; **C.** Sample R2923.

Fig. 7 The average Na occupancy of 8 symmetrically equivalent M sites in one unit cell (c~14Å) of all three samples. **A.** The average occupancy of sample Dul-15-8B is constant, indicating no density modulation in the structure; **B.** Sample SK90-12 shows a density modulation of ~8 mole% An; **C.** Sample R2923 shows a density modulation of ~17 mole% An.

Fig. 8 The average <T-O> bond distance of 8 symmetrically equivalent sites and total average of all 32 T sites in one unit cell (c~14Å) for all three samples. **A.** Sample Dul-15-8B; **B.** Sample SK90-12; **C.** Sample R2923.

Fig. 9 A section of the modulated structure consists of 3x7 anorthite cells along ***b***- and ***c***-axis. The modulation wavefront is marked with red plane in the figure. Oxygen atoms are omitted. Ca/Na atoms are shown as big spheres, with blue for Ca and yellow for Na occupancies. Al/Si atoms are shown as small spheres; Si occupancies are shown with dark blue color.

Fig. 10 M site and surrounding tetrahedra projected along ***a**** (A) and ***b**** (B) direction. The split M site lies within the plane defined by T_2 sites, which is parallel to the (100) plane. The split direction of the M site (green arrow) is close to the line connecting two diagonal T_2m-T_2o sites (red arrow).

Fig. 11 The split distances between M1 and M2 sites are plotted against the distances between diagonal T_2oz and T_2mo site for all three samples. The points for t=0 and t=0.5 are marked in red and green respectively. **A.** Sample Dul-15-8B; **B.** Sample SK90-12; **C.** Sample R2923.

675 Fig. 12 The modulation function of T_1o-O_A1-T_1m angle for all three samples. **A.** Sample Dul-15-
676 8B; **B.** Sample SK90-12; **C.** Sample R2923.

677

678 Fig. 13 Stereonet projection of the q-vectors of the three samples. The ***q***-vectors lie almost
679 exactly on the [923] zone-axis, tilting away from $(\bar{1}03)$ as the anorthite composition increases.
680 The stereonet is projected along the ***b***-axis, the same orientation as in Smith and Brown (1988).
681 Poles and traces of the two zone-axes [111] and $[\bar{5}1\bar{1}]$ used for dark-field images are also labeled
682 in the figure.

683

684 Fig. 14 Variations of selected modulation functions plotted against gamma angle of the structures
685 refined. Clear correlations between the parameters are shown.

686

687 Fig. 15 A schematic phase diagram around An_{51} showing topological relations of $C\bar{1}$, *e*1 and *e*2
688 phases. The gray area is where $C\bar{1}$ and *e*1 coexist as two thermodynamically stable phases,
689 which produce Bøggild intergrowth in extremely slow cooled igneous labradorite (which stayed
690 within the gray area long enough). The dash line is extended boundary between $C\bar{1}$ and *e*2, as *e*2
691 can appear with Ca-rich composition as a metastable phase. The loop area is modified from
692 McConnell (2008) considering compositions for two ends from Ribbe (1983a).

693

694 Fig. 16 A schematic time-temperature-transformation (TTT) diagram for plagioclase with
695 composition of ~An_{51}. Path A, B, C and D represent four host rock with gradually decreasing
696 cooling rate.

This is a preprint, the final version is subject to change, of the American Mineralogist (MSA)
Cite as Authors (Year) Title. American Mineralogist, in press.
(DOI will not work until issue is live.) DOI: http://dx.doi.org/10.2138/am-2017-6003

Fig. 1

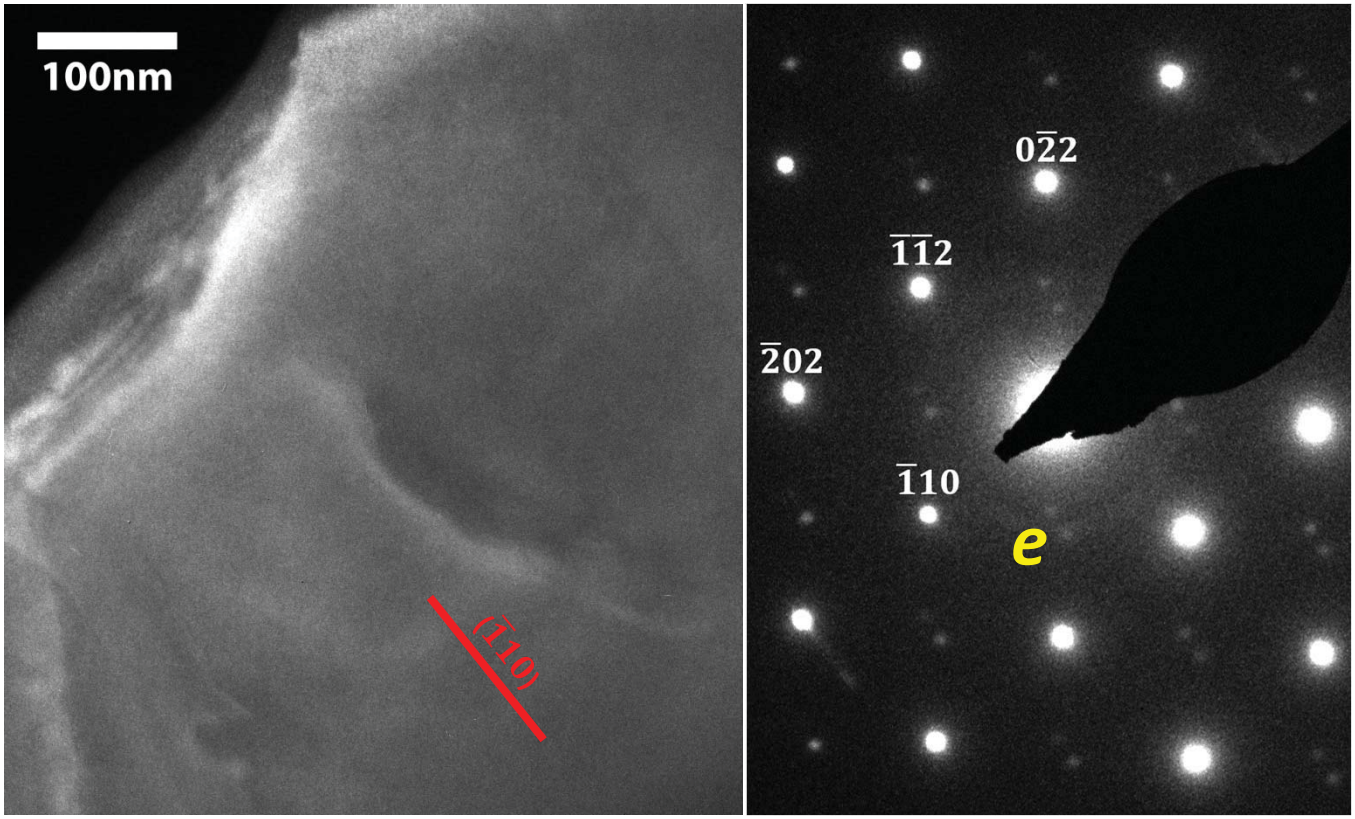

This is a preprint, the final version is subject to change, of the American Mineralogist (MSA)
Cite as Authors (Year) Title. American Mineralogist, in press.
(DOI will not work until issue is live.) DOI: http://dx.doi.org/10.2138/am-2017-6003

Fig. 2

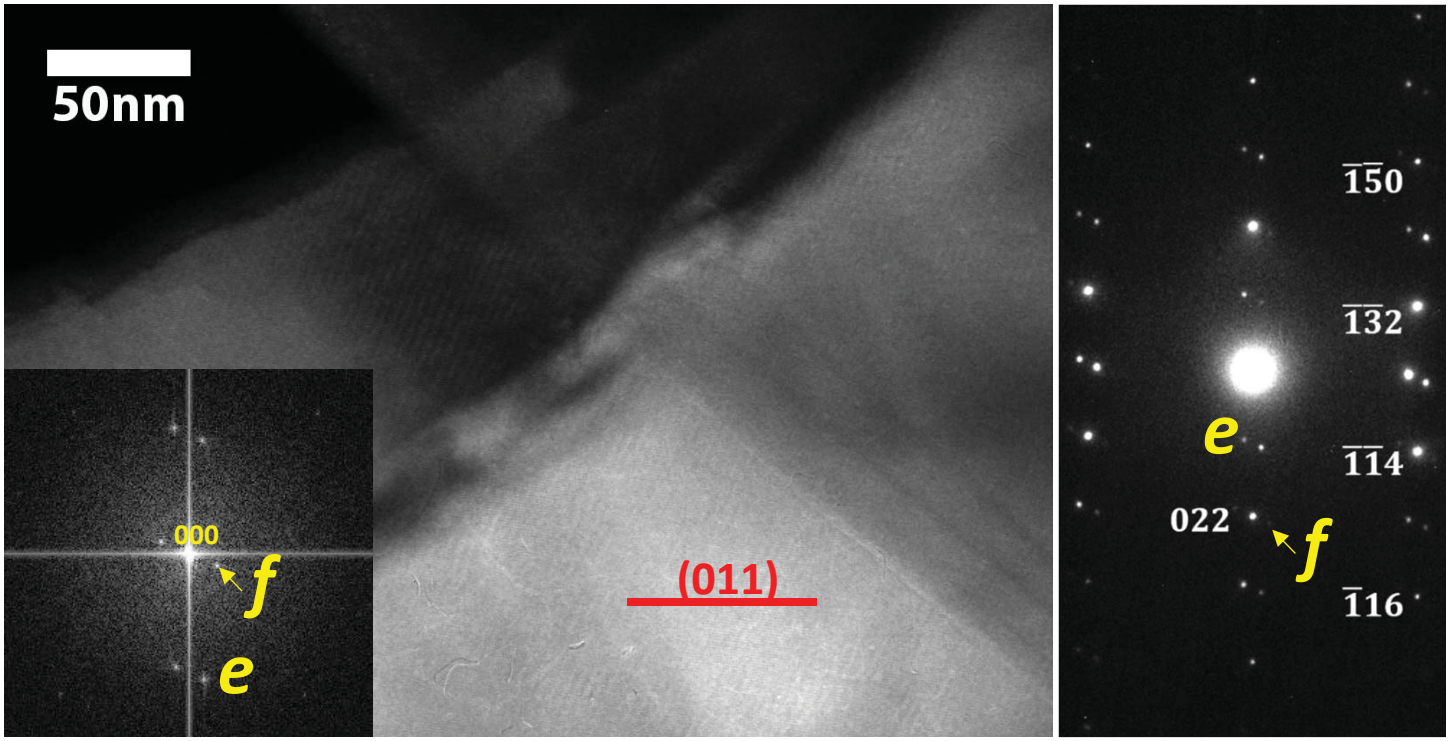

This is a preprint, the final version is subject to change, of the American Mineralogist (MSA)
Cite as Authors (Year) Title. American Mineralogist, in press.
(DOI will not work until issue is live.) DOI: http://dx.doi.org/10.2138/am-2017-6003

Fig. 3

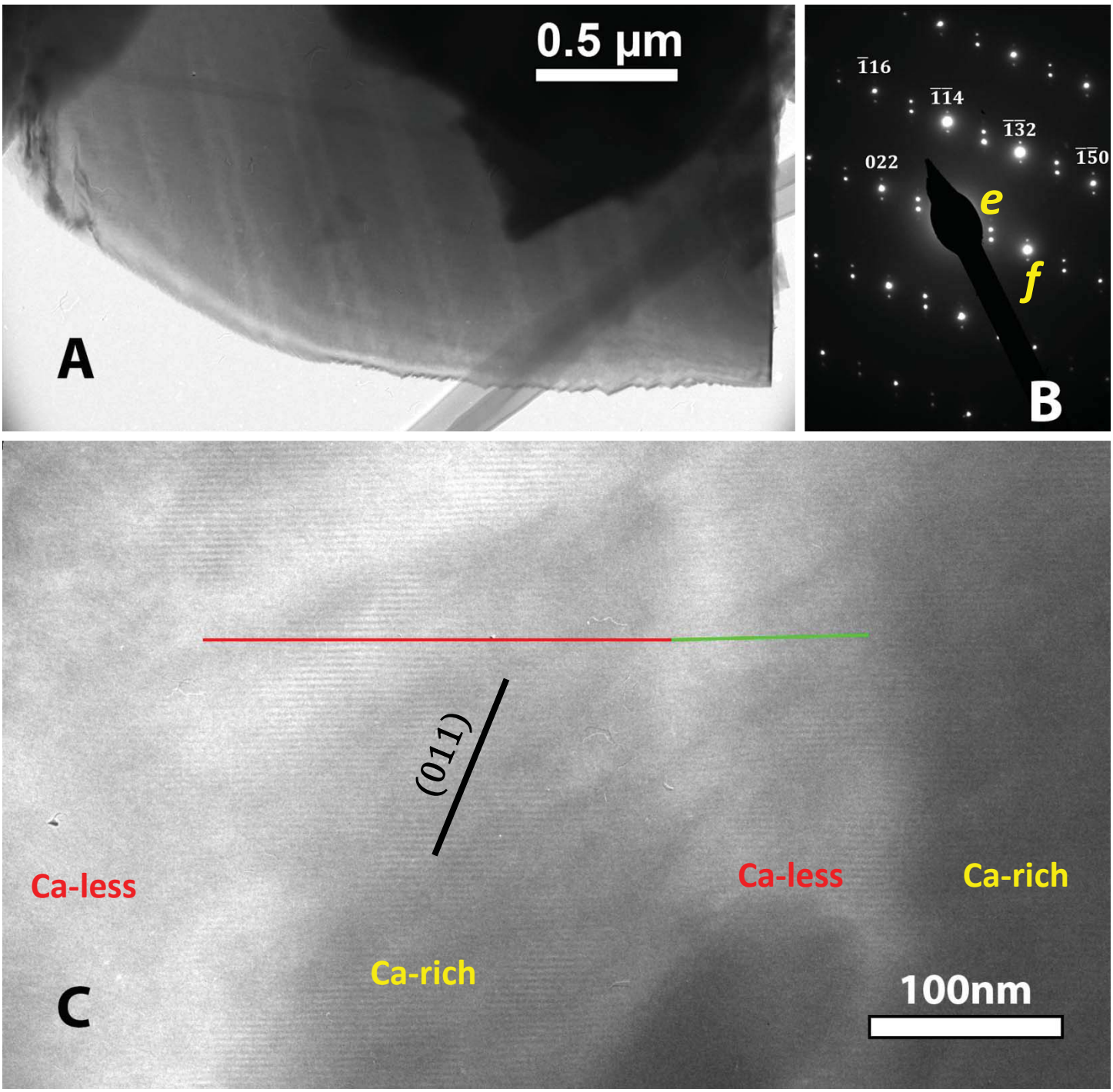

This is a preprint, the final version is subject to change, of the American Mineralogist (MSA)
Cite as Authors (Year) Title. American Mineralogist, in press.
(DOI will not work until issue is live.) DOI: http://dx.doi.org/10.2138/am-2017-6003

Fig. 4

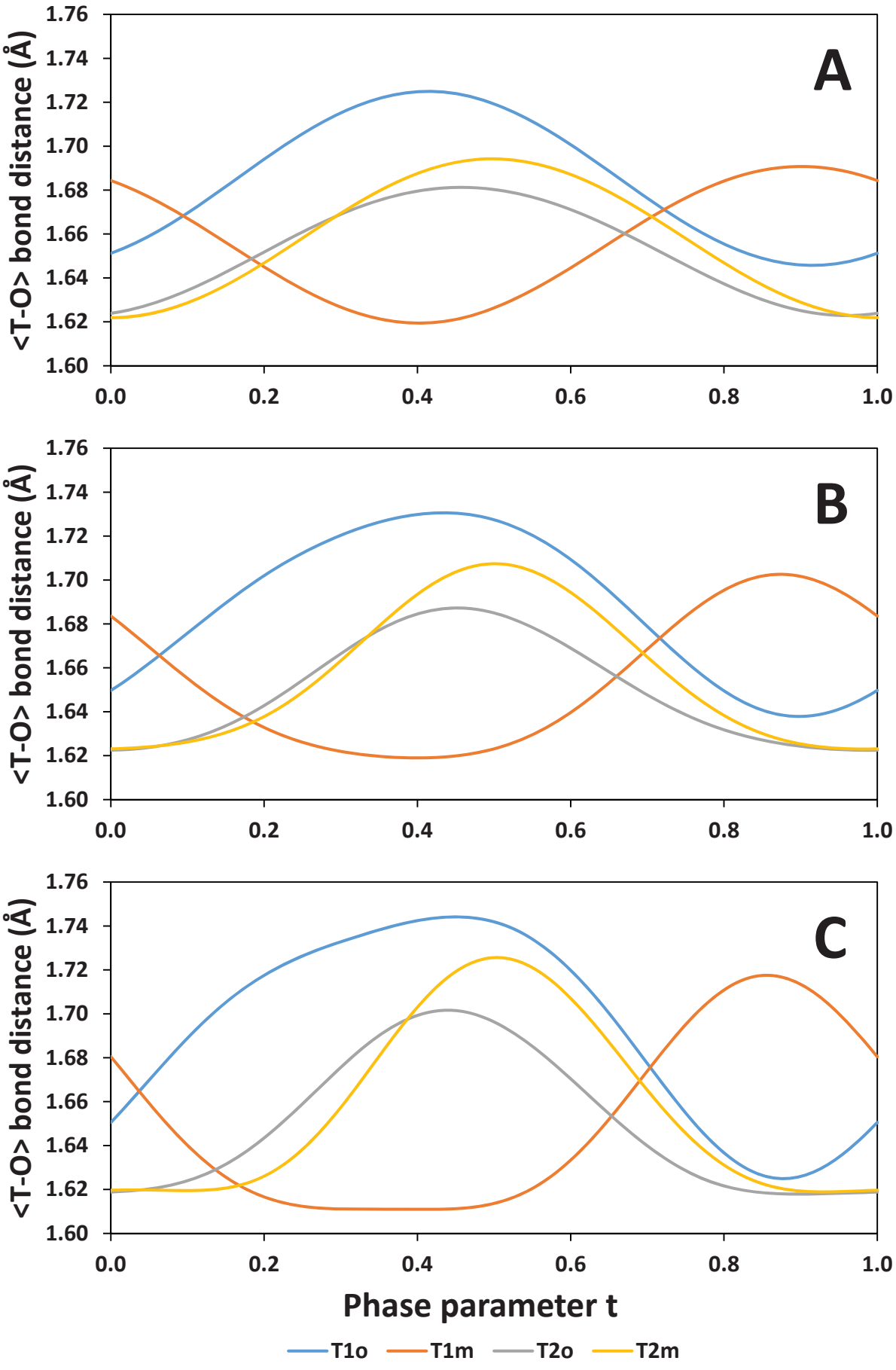

This is a preprint, the final version is subject to change, of the American Mineralogist (MSA)
Cite as Authors (Year) Title. American Mineralogist, in press.
(DOI will not work until issue is live.) DOI: http://dx.doi.org/10.2138/am-2017-6003

Fig. 5

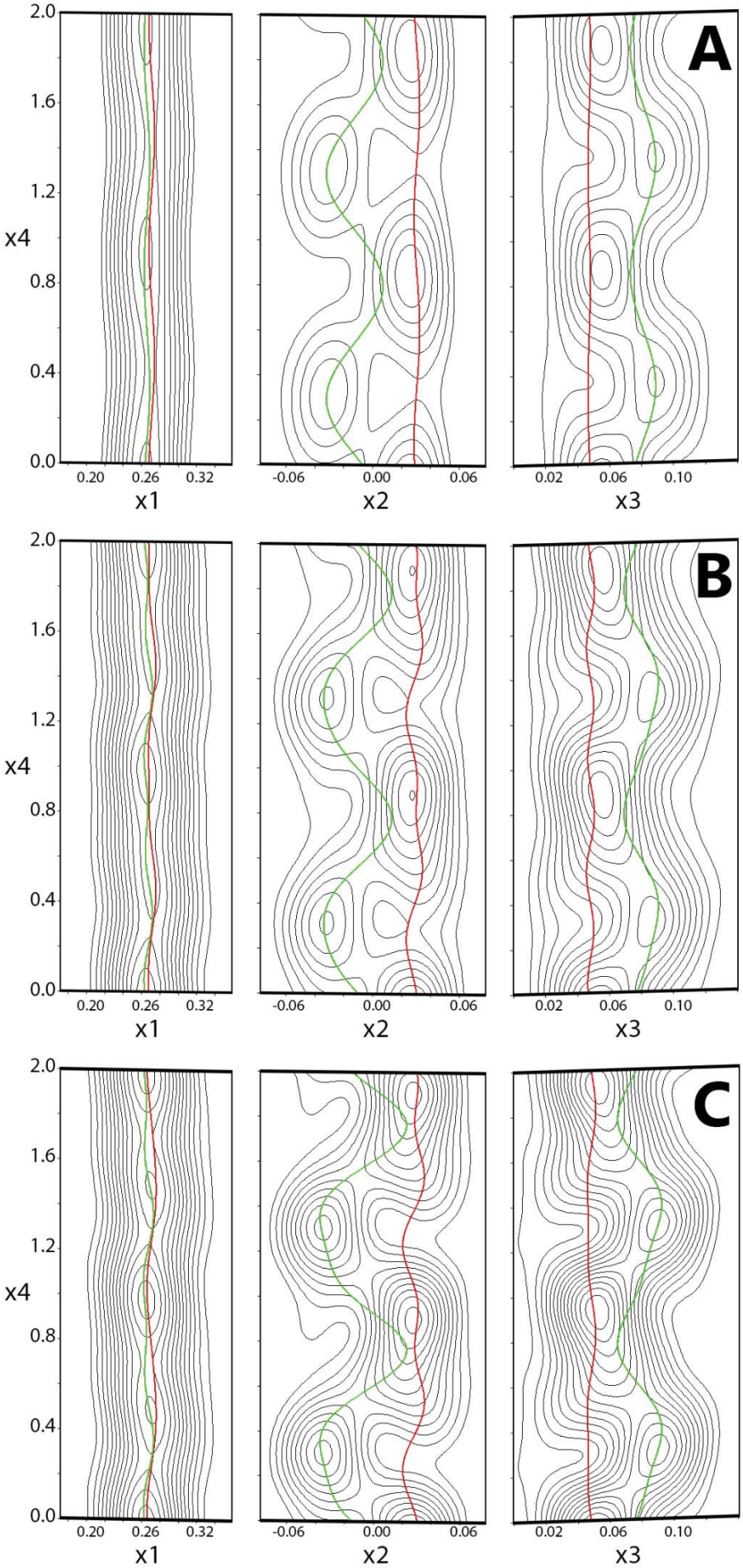

This is a preprint, the final version is subject to change, of the American Mineralogist (MSA)
Cite as Authors (Year) Title. American Mineralogist, in press.
(DOI will not work until issue is live.) DOI: http://dx.doi.org/10.2138/am-2017-6003

Fig. 6

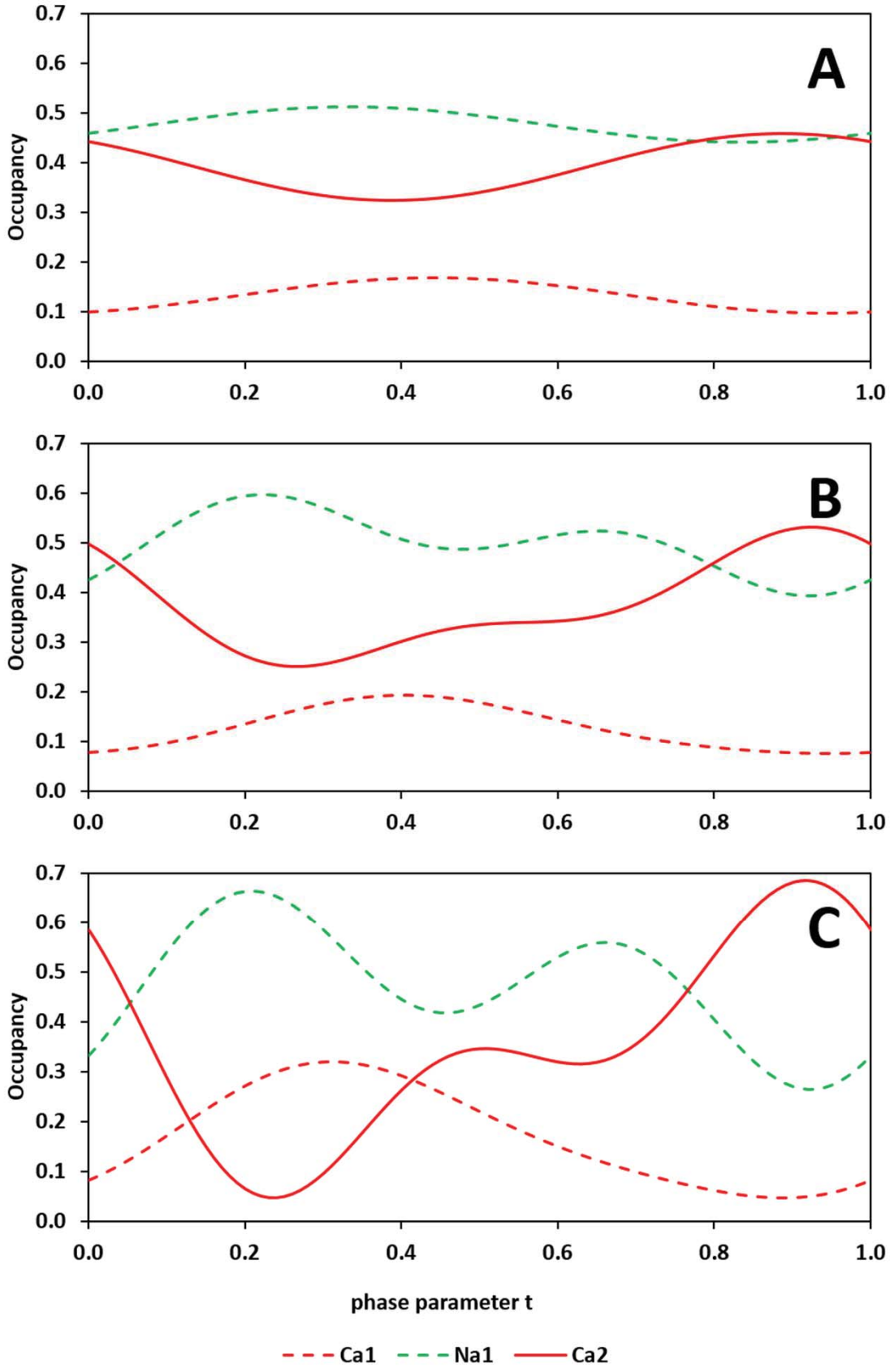

This is a preprint, the final version is subject to change, of the American Mineralogist (MSA)
Cite as Authors (Year) Title. American Mineralogist, in press.
(DOI will not work until issue is live.) DOI: http://dx.doi.org/10.2138/am-2017-6003

Fig. 7

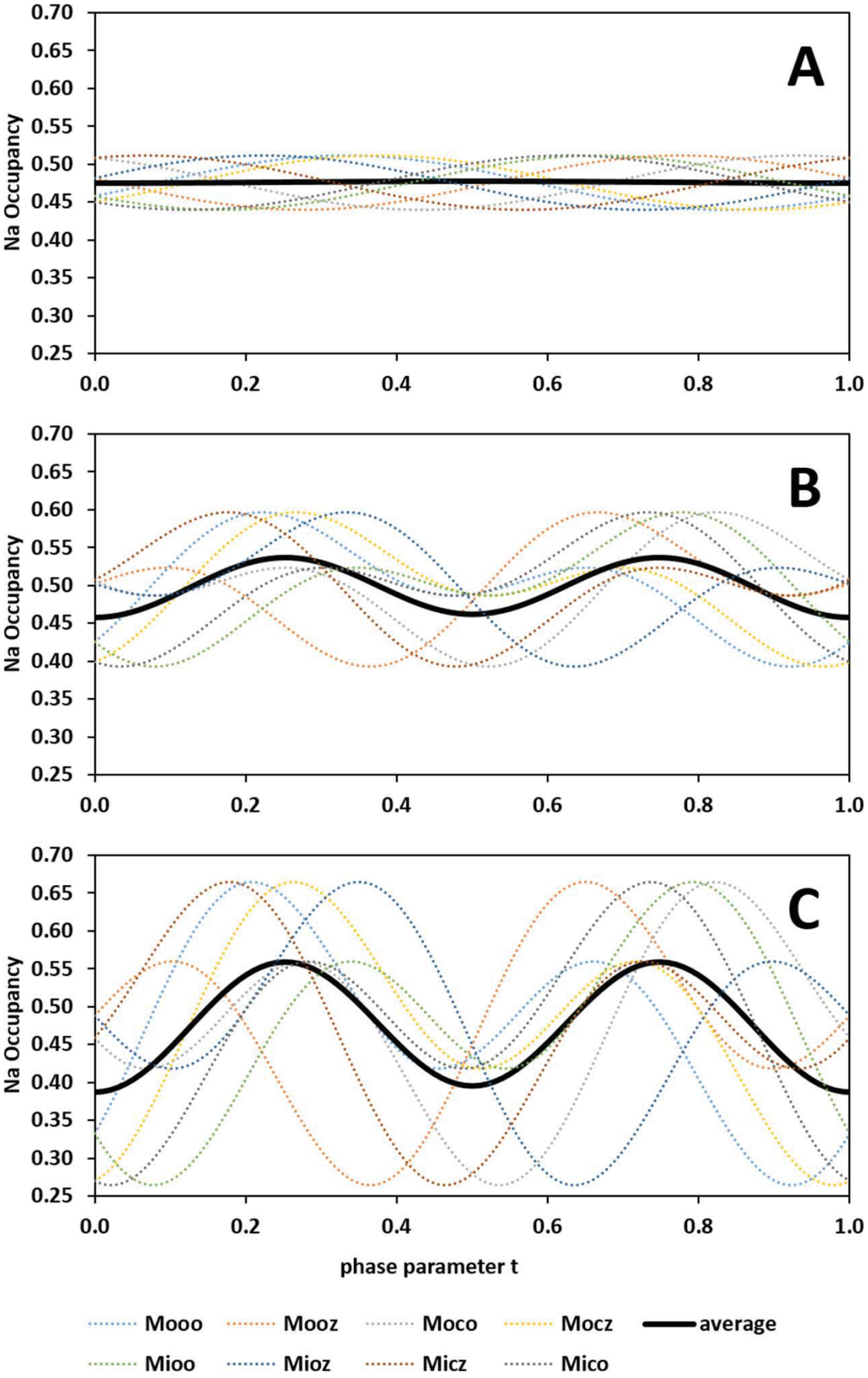

This is a preprint, the final version is subject to change, of the American Mineralogist (MSA)
Cite as Authors (Year) Title. American Mineralogist, in press.
(DOI will not work until issue is live.) DOI: http://dx.doi.org/10.2138/am-2017-6003

Fig. 8

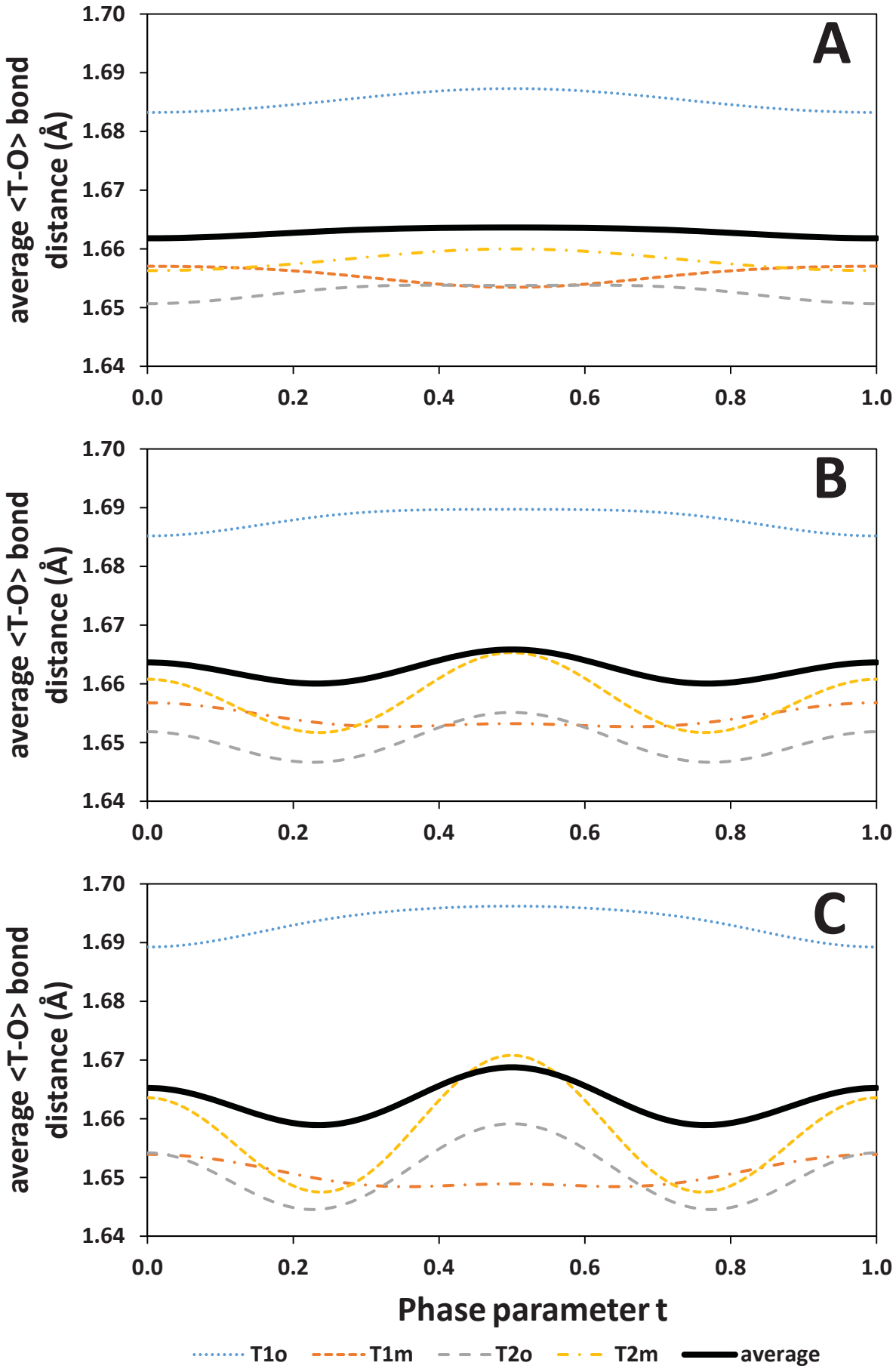

This is a preprint, the final version is subject to change, of the American Mineralogist (MSA)
Cite as Authors (Year) Title. American Mineralogist, in press.
(DOI will not work until issue is live.) DOI: http://dx.doi.org/10.2138/am-2017-6003

Fig. 9

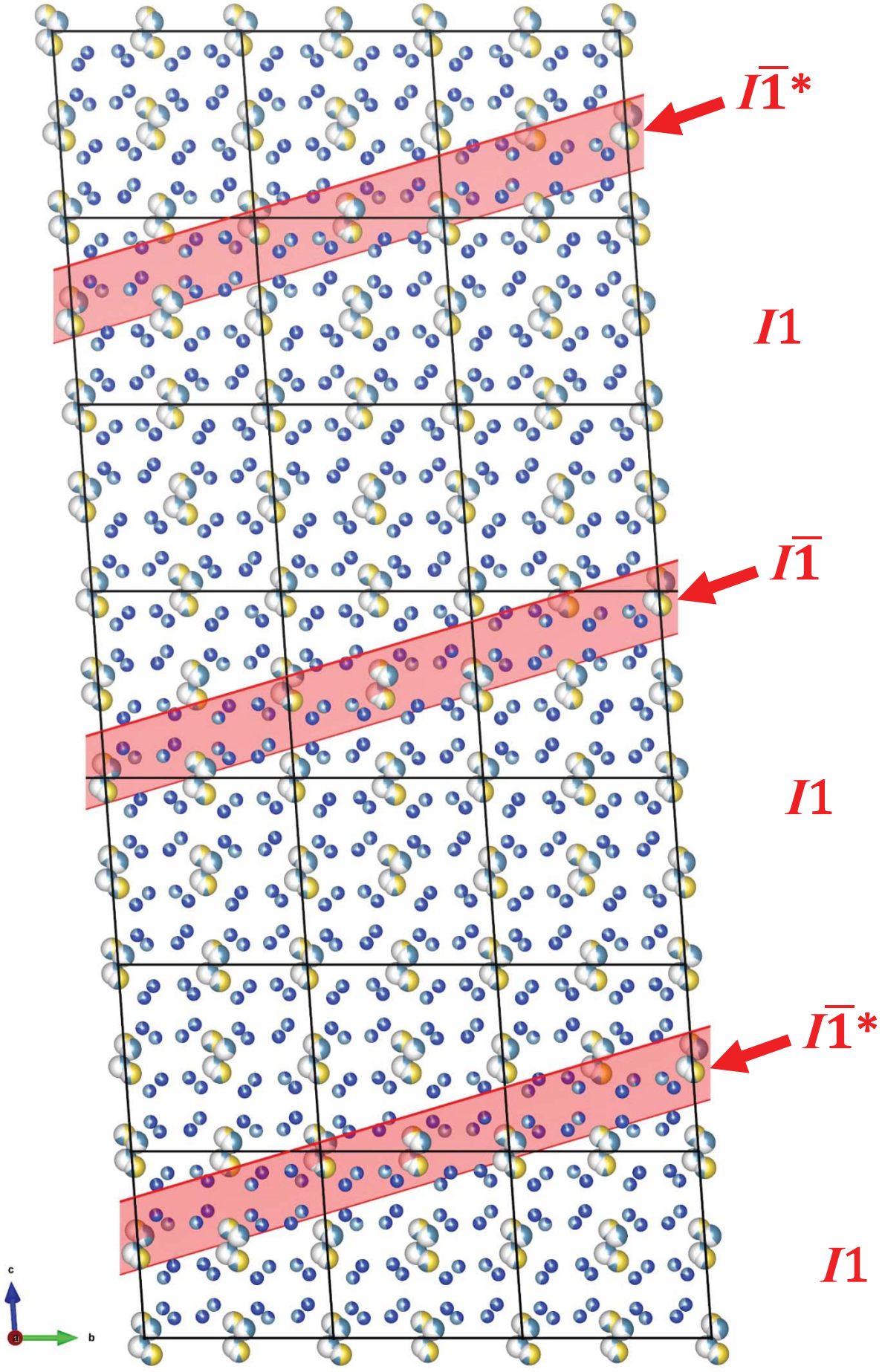

This is a preprint, the final version is subject to change, of the American Mineralogist (MSA)
Cite as Authors (Year) Title. American Mineralogist, in press.
(DOI will not work until issue is live.) DOI: http://dx.doi.org/10.2138/am-2017-6003

Fig. 10

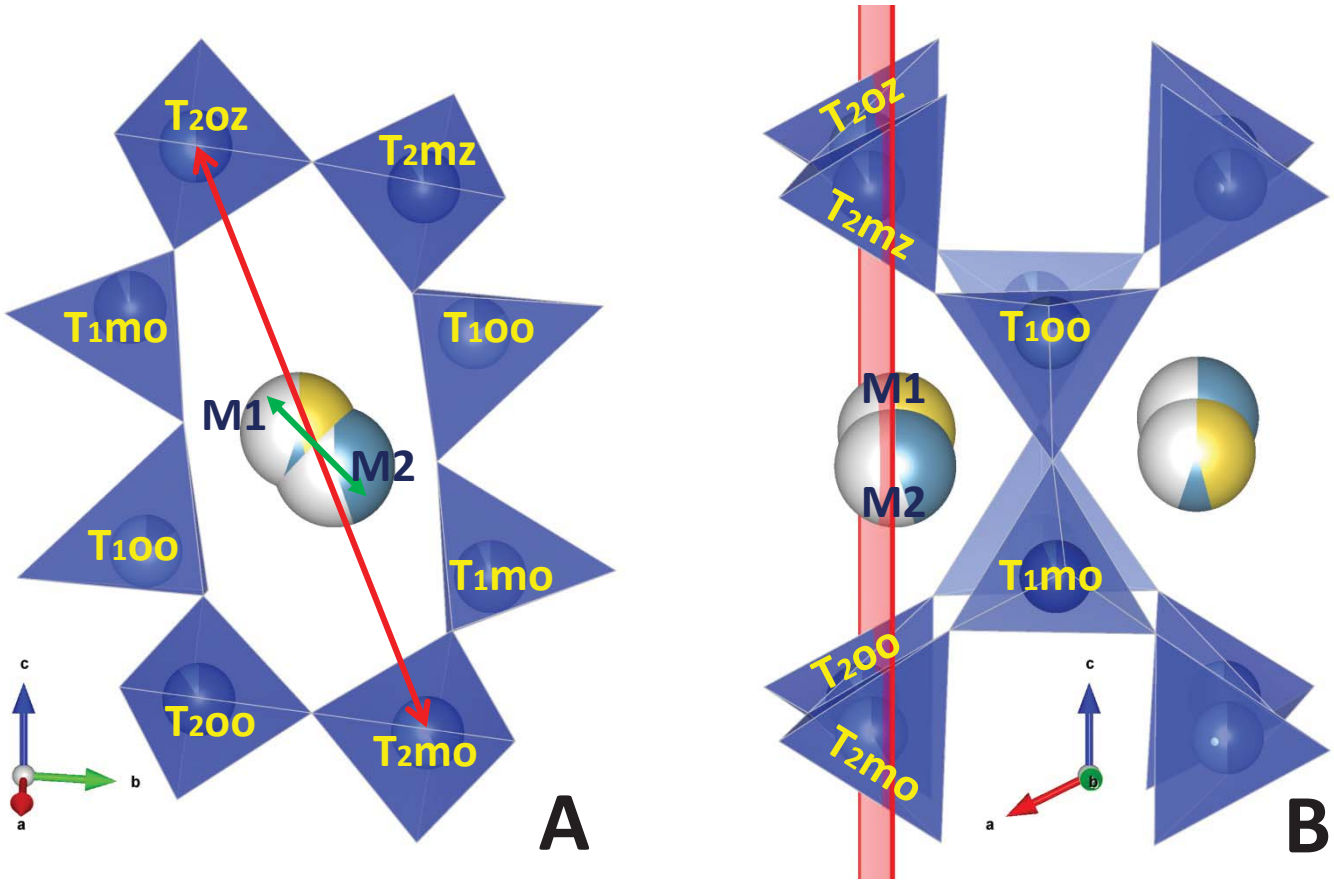

This is a preprint, the final version is subject to change, of the American Mineralogist (MSA)
Cite as Authors (Year) Title. American Mineralogist, in press.
(DOI will not work until issue is live.) DOI: http://dx.doi.org/10.2138/am-2017-6003

Fig. 11

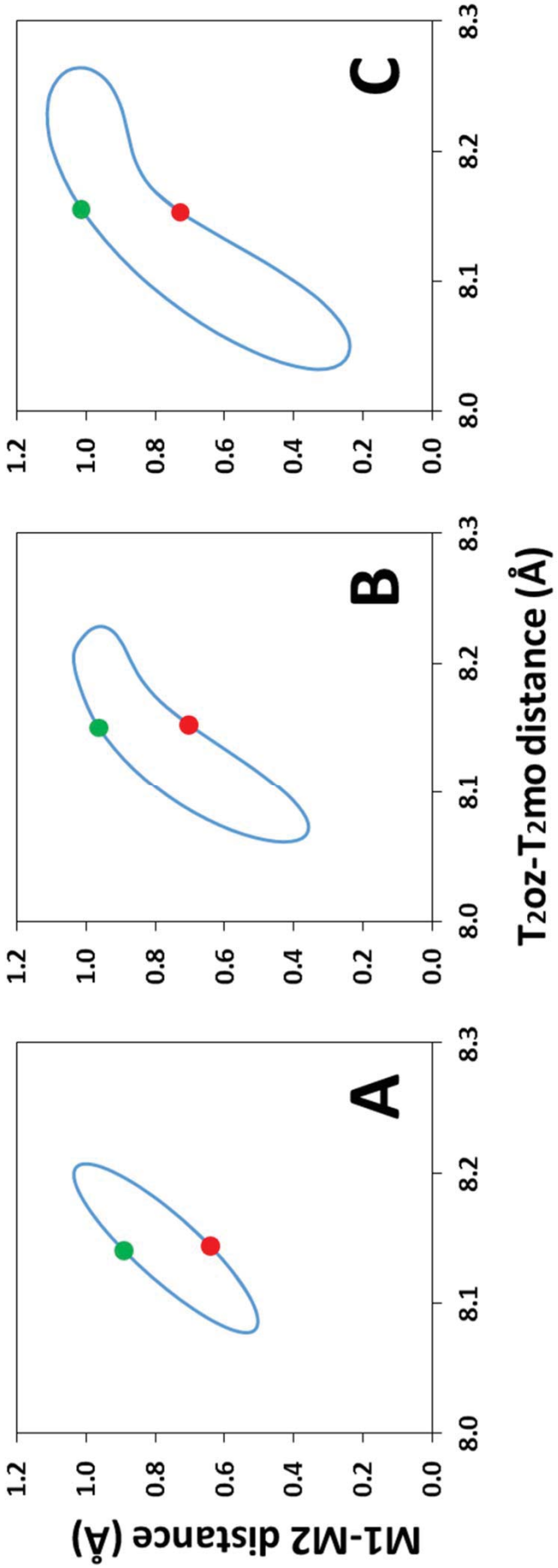

This is a preprint, the final version is subject to change, of the American Mineralogist (MSA)
Cite as Authors (Year) Title. American Mineralogist, in press.
(DOI will not work until issue is live.) DOI: http://dx.doi.org/10.2138/am-2017-6003

Fig. 12

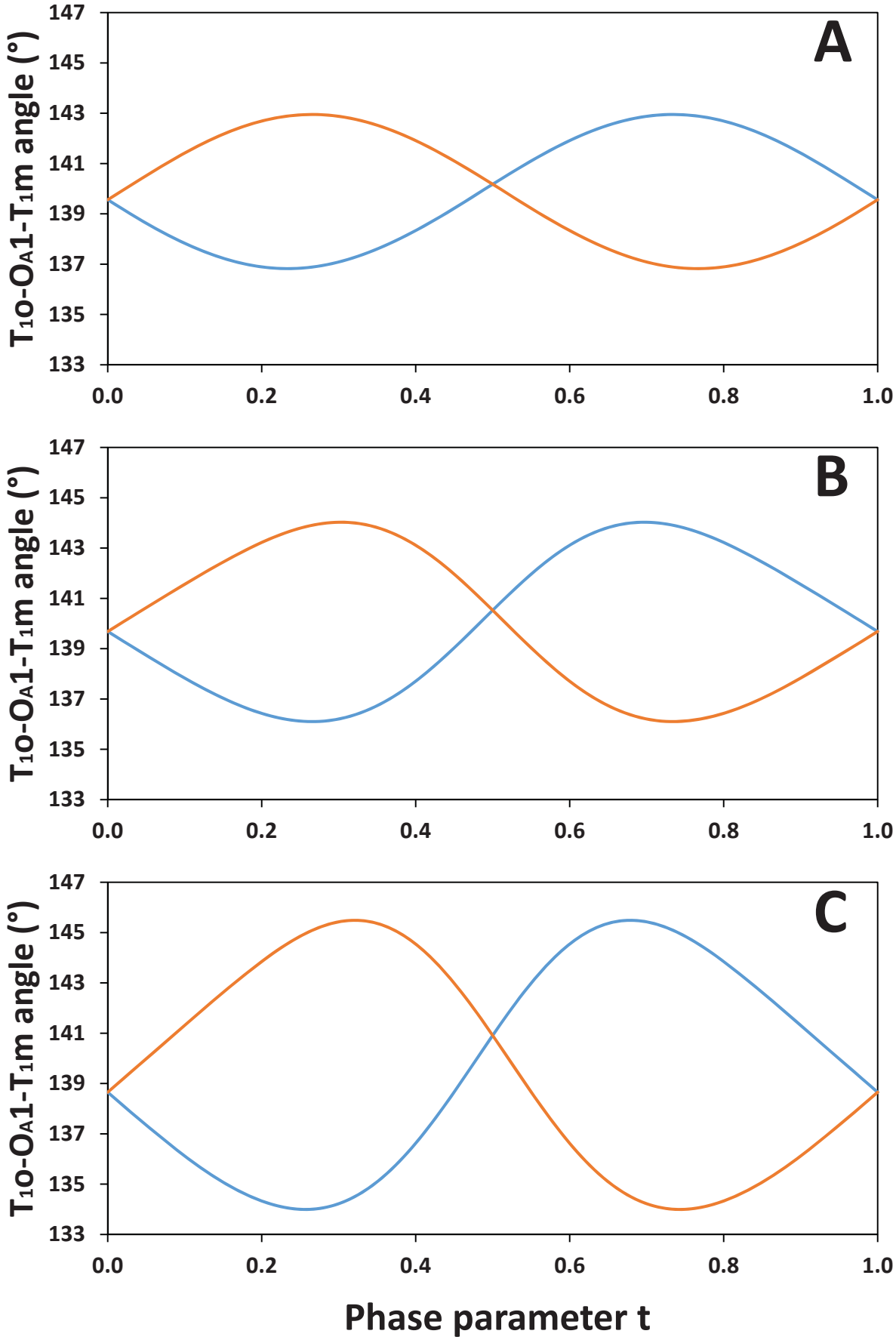

This is a preprint, the final version is subject to change, of the American Mineralogist (MSA)
Cite as Authors (Year) Title. American Mineralogist, in press.
(DOI will not work until issue is live.) DOI: http://dx.doi.org/10.2138/am-2017-6003

Fig. 13

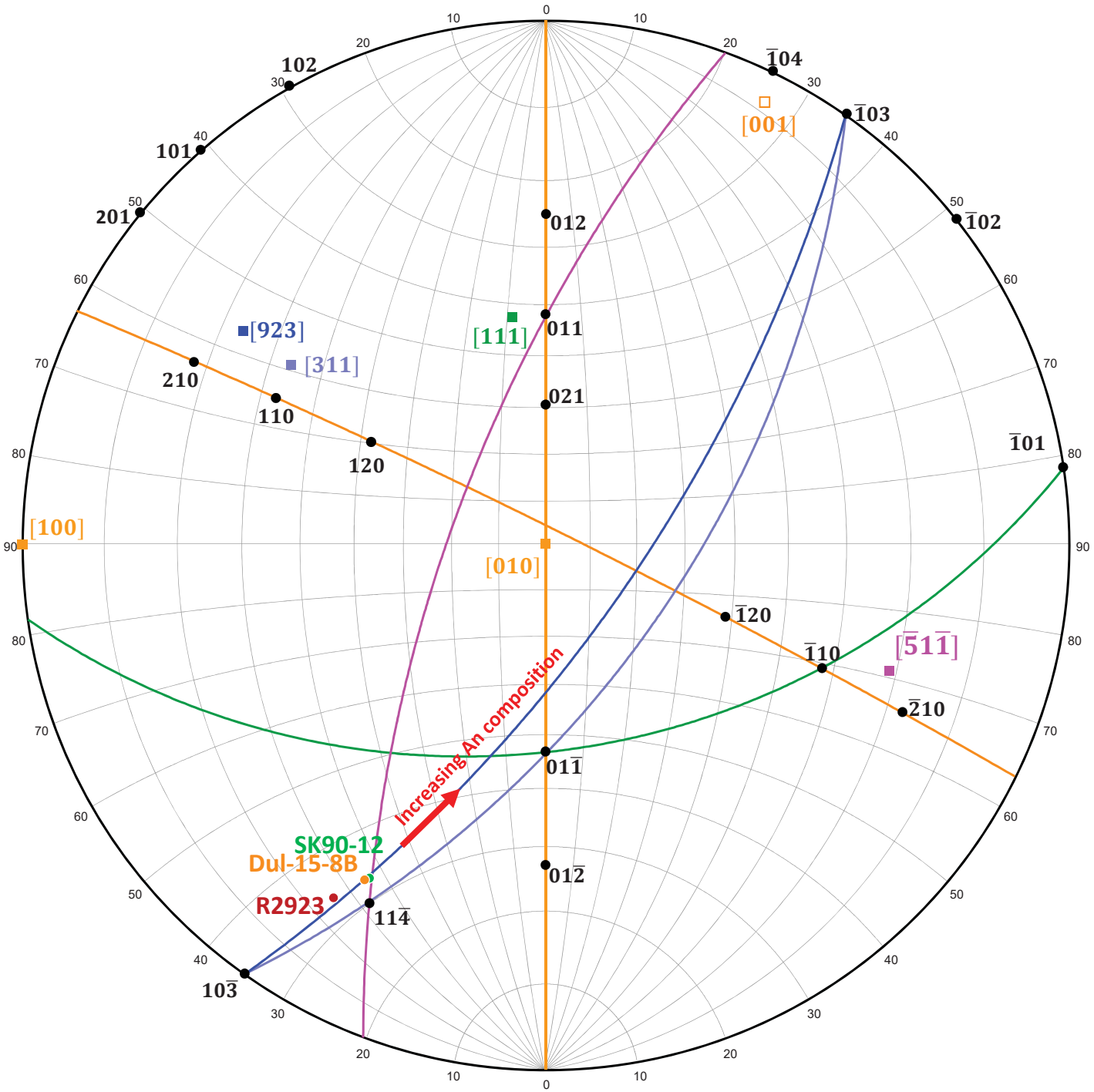

This is a preprint, the final version is subject to change, of the American Mineralogist (MSA)
Cite as Authors (Year) Title. American Mineralogist, in press.
(DOI will not work until issue is live.) DOI: http://dx.doi.org/10.2138/am-2017-6003

Fig. 14

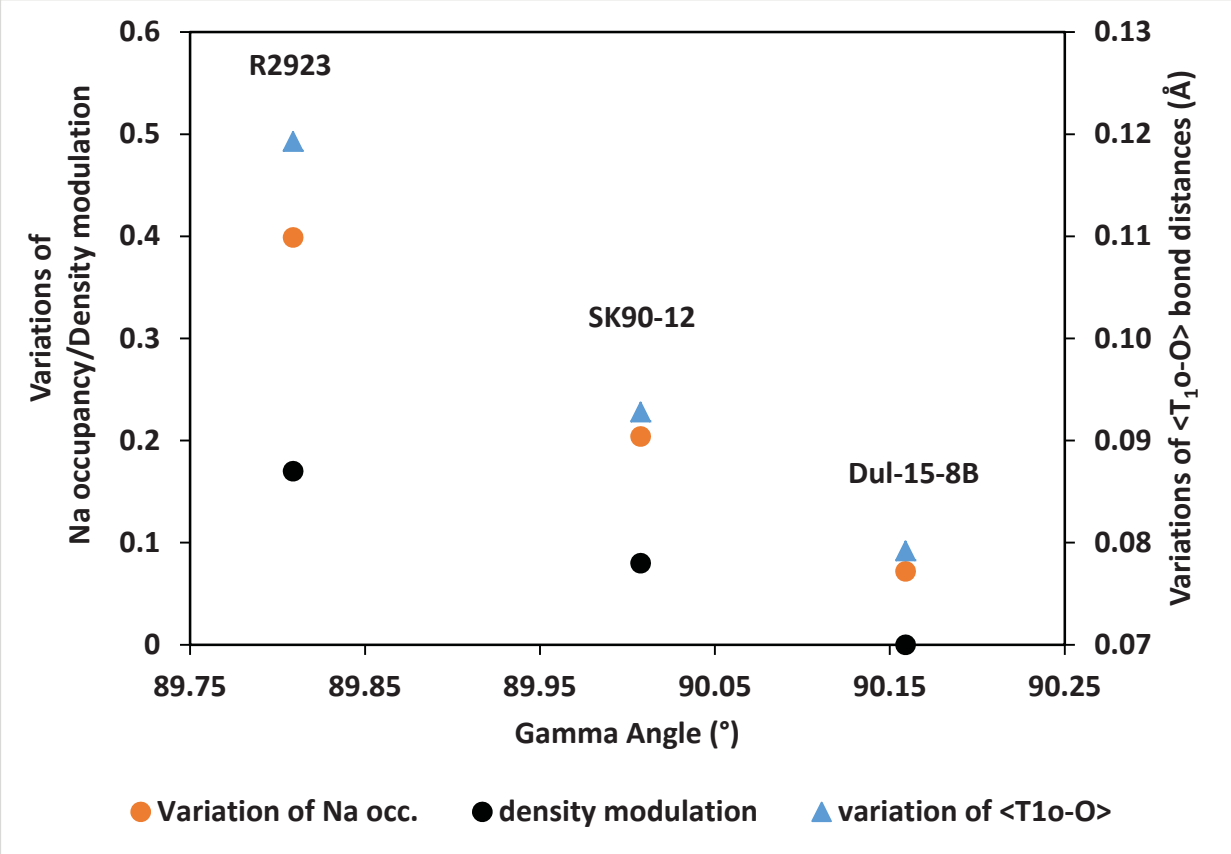

This is a preprint, the final version is subject to change, of the American Mineralogist (MSA)
Cite as Authors (Year) Title. American Mineralogist, in press.
(DOI will not work until issue is live.) DOI: http://dx.doi.org/10.2138/am-2017-6003

Fig. 15

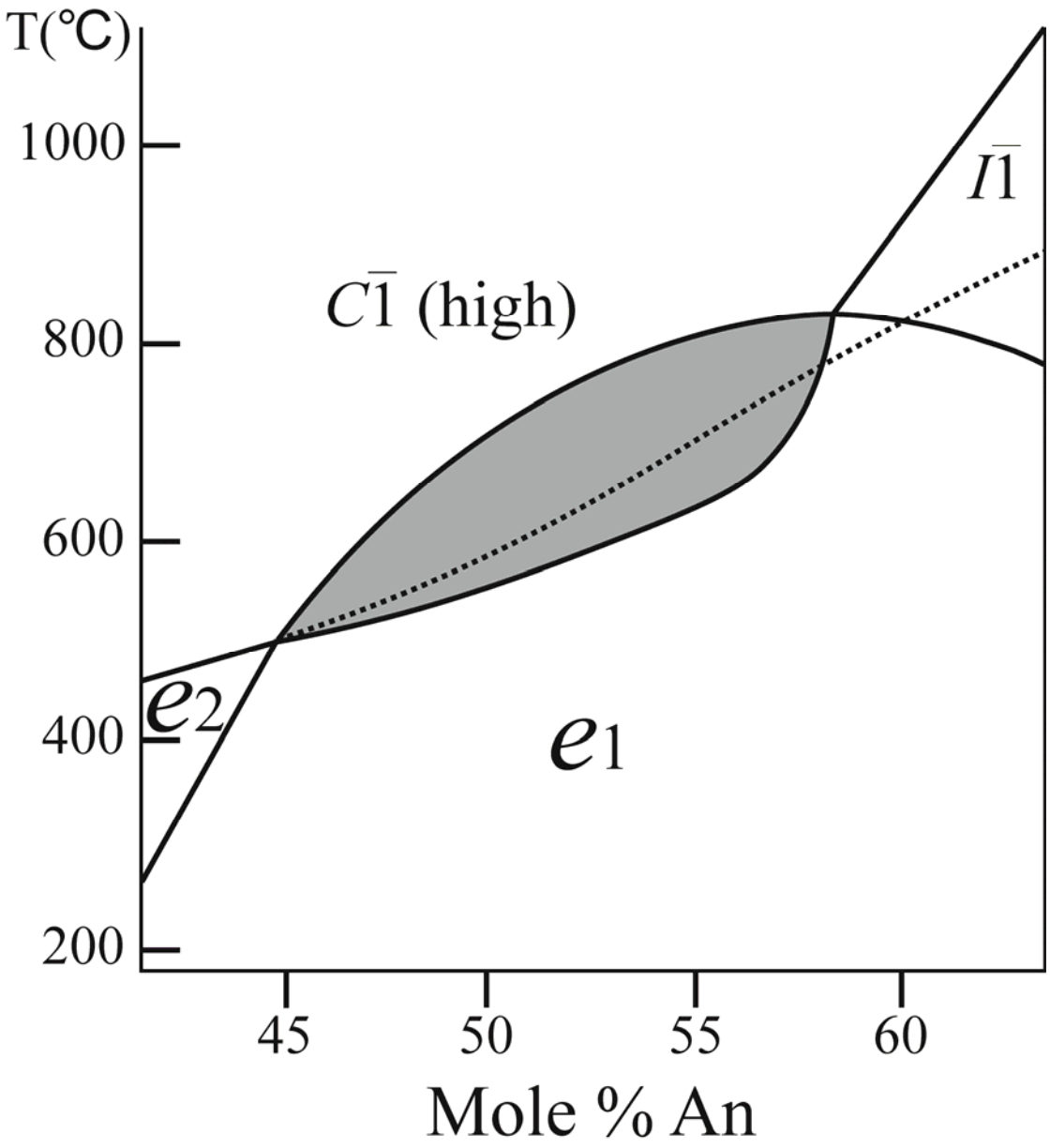

This is a preprint, the final version is subject to change, of the American Mineralogist (MSA)
Cite as Authors (Year) Title. American Mineralogist, in press.
(DOI will not work until issue is live.) DOI: http://dx.doi.org/10.2138/am-2017-6003

Fig. 16

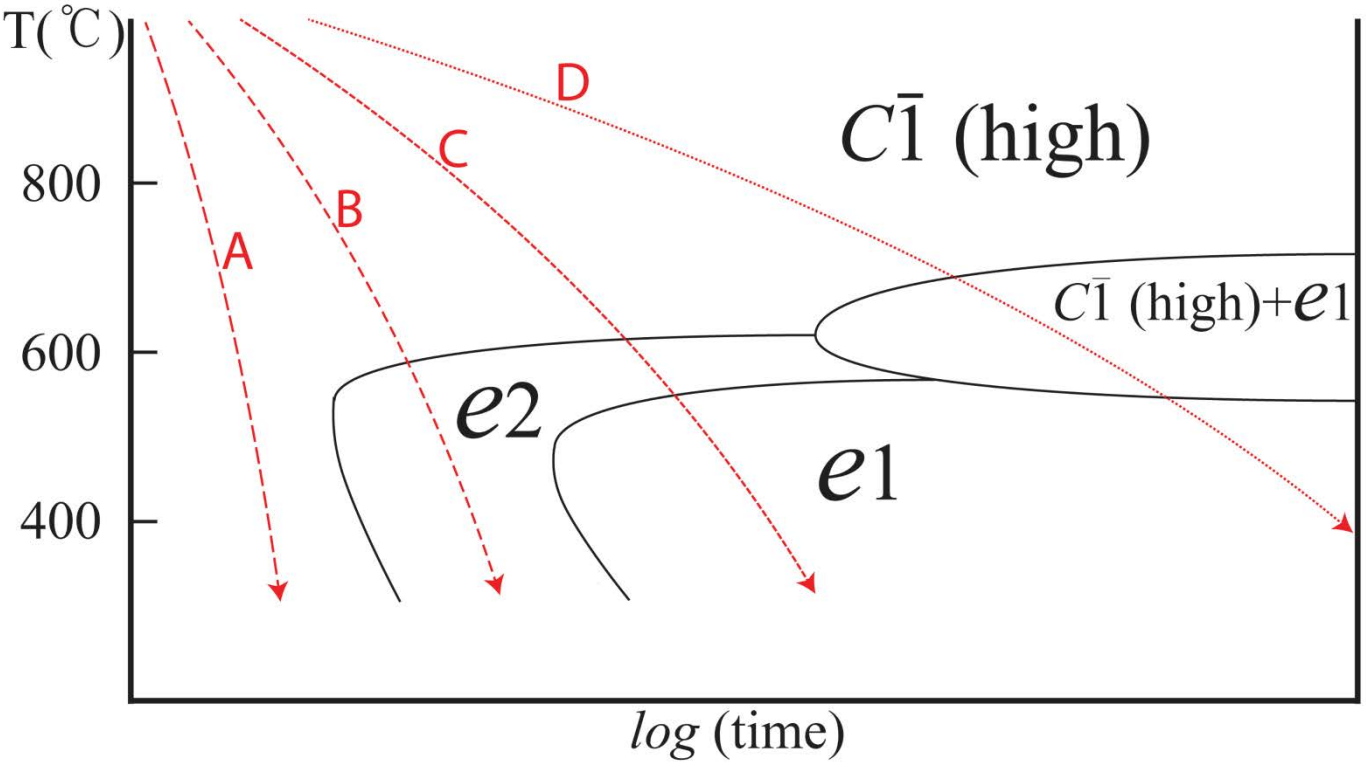

This is a preprint, the final version is subject to change, of the American Mineralogist (MSA)
Cite as Authors (Year) Title. American Mineralogist, in press.
(DOI will not work until issue is live.) DOI: http://dx.doi.org/10.2138/am-2017-6003

Table 1 Experimental details of the single crystal X-Ray diffraction analyses.

	Dul-15-8B	**SK90-12**	**R2923**
Crystal data			
Chemical formula	$Ca_{0.524}Na_{0.476}Si_{2.476}Al_{1.524}O_8$	$Ca_{0.501}Na_{0.499}Si_{2.5}Al_{1.5}O_8$	$Ca_{0.525}Na_{0.475}Si_{2.475}Al_{1.525}O_8$
M_r	270.6	270.2	270.6
Crystal system	Triclinic		
Space group	$X\bar{1}(\alpha\beta\gamma)0$[a]		
a, *b*, *c* (Å)	8.1625 (3), 12.8586 (2), 14.2038 (4)	8.1614 (1), 12.8545 (1), 14.2112 (2)	8.1658 (2), 12.8542 (1), 14.2096 (2)
α, β, γ (°)	93.5540 (7), 116.2161(2), 90.159 (3)	93.5904 (6), 116.2504 (9), 90.0075 (13)	93.6093 (7), 116.2726 (11), 89.8088 (14)
Wave vectors	δh = 0.05301(8) δk = 0.05905(8) δl = -0.20038(8)	δh = 0.05451(10) δk = 0.05751(10) δl = -0.20208(10)	δh = 0.06664(7) δk = 0.04916(7) δl = -0.22680(6)
Modulation period (Å)	33.95	34.07	30.75
V (Å^3)	1334.12 (7)	1333.88 (3)	1334.28 (4)
Crystal Size (mm^3)	0.116×0.100×0.089	0.086×0.077×0.061	0.139×0.115×0.093
F(000)	1074	1072	1074
D_x (Mg m^{-3})	2.694	2.691	2.694
μ (mm^{-1})	1.26	1.25	1.26
Data collection			
Radiation source	Mo Kα IμS		
Monochromator	Graphite		
Temperature	100K		
Total reflections measured	49534	40335	34735
Independent reflections	6091(2007*a*+4084*e*)[b]	10135(2028*a*+4074*e*+4033*f*)	8245(1649*a*+3316*e*+3280*f*)
Observed reflections	4975(1949*a*+3026*e*)	4613(1866*a*+2463*e*+284*f*)	5931(1600*a*+2779*e*+1552*f*)
R_{int}	0.042	0.138	0.047
θ values (°)	θ_{max} = 30.5, θ_{min} = 2.2	θ_{max} = 30.5, θ_{min} = 2.0	θ_{max} = 28.3, θ_{min} = 1.9
$(\sin\theta/\lambda)_{max}$ (Å^{-1})	0.715	0.715	0.667
Range of *h*, *k*, *l*	*h* = -11→11, *k* = -18→18, *l* = -20→20	*h* = -11→11, *k* = -18→18, *l* = -20→20	*h* = -11→10, *k* = -17→17, *l* = -19→19

This is a preprint, the final version is subject to change, of the American Mineralogist (MSA)
Cite as Authors (Year) Title. American Mineralogist, in press.
(DOI will not work until issue is live.) DOI: http://dx.doi.org/10.2138/am-2017-6003

Refinement			
Refined on	F^2		
$R[F^2 > 2\sigma(F^2)]$	0.029(0.023/0.048)[c]	0.033(0.030/0.034/0.132)	0.032(0.028/0.032/0.076)
R(*all*)	0.037(0.024/0.072)	0.064(0.032/0.061/0.380)	0.042(0.028/0.039/0.142)
GOF(obs)	2.67	1.62	1.93
GOF(all)	2.43	1.12	1.66
No. of parameters	385	640	604
No. of constraints	150	250	239
Weighting scheme	Weighting scheme based on measured s.u.'s $w = 1/(\sigma^2(I) + 0.0004I^2)$		
$(\Delta/\sigma)_{max}$	0.030	0.037	0.021

[a] Centering condition X: (½,½,½,0),(½,½,0,½),(0,0,½,½), corresponding to C_c' in *Table 3.9* of (van Smaalen, 2007)

[b] Letter *a* and *e* (and *f*, if present) refer to main reflections and first order satellites (and second order satellites)

[c] Values in parentheses refer to R for *a* and *e* (and *f* reflections, if present) respectively

Table 2 Atomic positions and occupancies in the modulated structure of sample Dul-15-8B. Note that all the fractional coordinates are based on **c**~14Å unit cell, even though the number of independent atoms is the same as in albite cell (**c**~7 Å)

label	atom	Average Occ.	Max Occ.	Min Occ.	X	y	z	Uequiv
M1	Ca	0.133(5)	0.169	0.098	0.26625(11)	-0.01220(3)	0.08100(2)	0.0280(6)
	Na	0.476(3)	0.512	0.440				
M2	Ca	0.391(6)	0.458	0.324	0.27157(10)	0.03077(7)	0.04735(9)	0.0134(3)
T_1o	Si	0.4535	0.747	0.160	0.49373(4)	0.33644(2)	-0.10713(2)	0.00656(10)
	Al	0.5465	0.840	0.253				
T_1m	Si	0.6736	0.938	0.409	0.50308(4)	0.31684(2)	0.11573(2)	0.00687(10)
	Al	0.3264	0.591	0.062				
T_2o	Si	0.6943	0.910	0.478	0.68514(4)	0.10875(2)	0.15822(2)	0.00679(10)
	Al	0.3057	0.522	0.090				
T_2m	Si	0.6546	0.923	0.387	0.18086(4)	0.37894(2)	0.17851(2)	0.00656(10)
	Al	0.3453	0.613	0.077				
O_A1	O	1			0.49740(12)	0.37132(6)	0.01064(6)	0.0160(3)
O_A2	O	1			0.57988(10)	-0.00812(6)	0.13892(6)	0.0101(2)
O_Bo	O	1			0.81245(11)	0.10394(6)	0.09430(7)	0.0146(3)
O_Bm	O	1			0.31592(11)	0.35283(7)	0.12231(8)	0.0202(3)
O_Co	O	1			0.48665(11)	0.20938(6)	-0.14032(6)	0.0135(3)
O_Cm	O	1			0.51385(11)	0.18786(6)	0.10648(6)	0.0148(3)
O_Do	O	1			0.30173(10)	0.39288(6)	0.30853(6)	0.0134(3)
O_Dm	O	1			0.69006(11)	0.36635(6)	0.21588(6)	0.0164(3)

This is a preprint, the final version is subject to change, of the American Mineralogist (MSA)
Cite as Authors (Year) Title. American Mineralogist, in press.
(DOI will not work until issue is live.) DOI: http://dx.doi.org/10.2138/am-2017-6003

Table 3 Atomic positions and occupancies in the modulated structure of sample SK90-12.

label	atom	Average Occ.	Max Occ.	Min Occ.	x	y	z	Uequiv
M1	Ca	0.129(9)	0.193	0.075	0.26698(15)	-0.01241(12)	0.08054(10)	0.0288(5)
	Na	0.499(12)	0.596	0.392				
M2	Ca	0.371(8)	0.532	0.250	0.27103(14)	0.02970(9)	0.04829(9)	0.0173(3)
T1o	Si	0.4397	0.830	0.113	0.49383(3)	0.33619(2)	-0.10698(2)	0.00784(9)
	Al	0.5603	0.887	0.170				
T1m	Si	0.6830	0.960	0.312	0.50302(3)	0.31716(2)	0.11584(2)	0.00801(9)
	Al	0.3170	0.688	0.040				
T2o	Si	0.7149	0.931	0.425	0.68524(3)	0.10878(2)	0.15808(2)	0.00783(9)
	Al	0.2851	0.575	0.069				
T2m	Si	0.6624	0.930	0.277	0.18094(3)	0.37915(2)	0.17853(2)	0.00760(9)
	Al	0.3376	0.723	0.070				
O_A1	O	1			0.49757(10)	0.37118(5)	0.01087(5)	0.0164(3)
O_A2	O	1			0.58015(9)	-0.00768(5)	0.13883(5)	0.0109(2)
O_Bo	O	1			0.81201(9)	0.10437(5)	0.09420(6)	0.0151(2)
O_Bm	O	1			0.31603(10)	0.35282(6)	0.12255(6)	0.0201(3)
O_Co	O	1			0.48687(9)	0.20888(6)	-0.14006(5)	0.0145(2)
O_Cm	O	1			0.51433(9)	0.18826(6)	0.10685(5)	0.0160(2)
O_Do	O	1			0.30143(9)	0.39273(5)	0.30838(5)	0.0142(2)
O_Dm	O	1			0.69009(9)	0.36674(5)	0.21611(6)	0.0168(2)

This is a preprint, the final version is subject to change, of the American Mineralogist (MSA)
Cite as Authors (Year) Title. American Mineralogist, in press.
(DOI will not work until issue is live.) DOI: http://dx.doi.org/10.2138/am-2017-6003

Table 4 Atomic positions and occupancies in the modulated structure of sample R2923.

label	atom	Average Occ.	Max Occ.	Min Occ.	x	y	z	Uequiv
M1	Ca	0.171(2)	0.319	0.047	0.26670(13)	-0.01331(17)	0.08044(15)	0.0244(4)
	Na	0.475(3)	0.664	0.265				
M2	Ca	0.354(2)	0.685	0.048	0.27123(14)	0.02886(9)	0.04801(9)	0.0089(2)
T_1o	Si	0.3944	0.898	0.021	0.49380(4)	0.33570(2)	-0.10684(2)	0.00632(11)
	Al	0.6056	0.979	0.102				
T_1m	Si	0.7054	0.994	0.213	0.50308(4)	0.31772(2)	0.11606(2)	0.00634(10)
	Al	0.2946	0.787	0.006				
T_2o	Si	0.7110	0.954	0.334	0.68532(4)	0.10907(2)	0.15793(2)	0.00642(11)
	Al	0.2890	0.666	0.046				
T_2m	Si	0.6642	0.944	0.160	0.18113(4)	0.37948(2)	0.17858(2)	0.00631(11)
	Al	0.3358	0.840	0.056				
O_A1	O	1			0.49761(11)	0.37165(6)	0.01149(6)	0.0145(3)
O_A2	O	1			0.58061(10)	-0.00708(6)	0.13887(6)	0.0096(3)
O_Bo	O	1			0.81203(10)	0.10514(6)	0.09420(6)	0.0131(3)
O_Bm	O	1			0.31686(11)	0.35299(7)	0.12310(7)	0.0180(3)
O_Co	O	1			0.48713(10)	0.20793(6)	-0.13962(6)	0.0123(3)
O_Cm	O	1			0.51516(10)	0.18927(6)	0.10754(6)	0.0136(3)
O_Do	O	1			0.30094(10)	0.39289(6)	0.30824(6)	0.0124(3)
O_Dm	O	1			0.68940(11)	0.36694(6)	0.21607(6)	0.0153(3)

This is a preprint, the final version is subject to change, of the American Mineralogist (MSA)
Cite as Authors (Year) Title. American Mineralogist, in press.
(DOI will not work until issue is live.) DOI: http://dx.doi.org/10.2138/am-2017-6003

Table 5 Potential parameters for estimating the ordering state of e-plagioclase

	Dul-15-8B	SK90-12	R2923	987L[a]
Composition	An_{52}	An_{50}	An_{52}	An_{51}
Gamma (°)	90.159	90.008	89.809	89.840[b]
Modulation Period (Å)	33.95	34.07	30.75	30.15[c]
Modulation	*e*2	*e*1	*e*1+*e*1	*e*1
Na occ. variation (peak-trough)	0.072	0.204	0.399	0.353
Density variation (mole% An)	0	8	17	17
Average $<T_1o - O>$ (Å)	1.6852	1.6876	1.6935	1.6907
Average $<T_1m - O>$ (Å)	1.6555	1.6547	1.6516	1.6508
Average $<T_2o - O>$ (Å)	1.6527	1.6504	1.6508	1.6474
Average $<T_2m - O>$ (Å)	1.6581	1.6575	1.6571	1.6562
$<T_1o-O>$ variation (Å)	0.0790	0.0928	0.1193	0.1170
$<T_1m-O>$ variation (Å)	0.0713	0.0836	0.1066	0.1066
$<T_2o-O>$ variation (Å)	0.0584	0.0648	0.0837	0.0842
$<T_2m-O>$ variation (Å)	0.0724	0.0844	0.1067	0.1090

[a] Metamorphic labradorite with no exsolution, data collected at room temperature (Jin and Xu, 2017).

[b] For comparison, the unit cell parameters **(**a, b, c, α, β, γ**)** of the same crystal were measured to be **(**8.1610(1) Å, 12.8481(1) Å, 14.2074(2) Å, 93.6469(6)°, 116.2616(9)°, 89.8744(13)°**)** at 100K.

[c] The *q*-vector **(**δ*h*, δ*k*, δ*l***)** measured at 100K was **(**0.06667, 0.05477, 0.2293**)**, resulting in a period of 30.29 Å.